

Black Hole Shadows in General Relativity and Tensor-Multi-Scalar Theories of Gravity

by Ayush Roy

Supervised by: Dr. Daniela Doneva

A thesis submitted in partial fulfillment of the requirements
for the degree of Master of Science in Mathematical Physics

Eberhard Karls Universität Tübingen
August 7, 2023

Declaration

Ich Ayush Roy (Matrikel Nr. 6016838) versichere,

1. dass Ich diese Arbeit selbständig verfasst habe,
2. dass Ich keine anderen als die angegebenen Hilfsmittel und Quellen benutzt habe,
3. dass Ich wörtliche oder sinngemäß aus anderen Werken übernommene Aussagen als solche gekennzeichnet habe,
4. dass die Arbeit bisher weder gesamt noch in Teilen einer anderen Prüfungsbehörde vorgelegt wurde,
5. dass das in Dateiform eingereichte Exemplar mit dem eingereichten gebundenen Exemplar übereinstimmt.

Tübingen, August 7, 2023,

Ayush Roy

Acknowledgements

I would like to thank my parents for financially supporting my journey on the gravitational physics manifold till now.

Academically, Dr. Daniela Doneva has been the dream supervisor; her keenness to address questions and problems in a timely manner along with her constant stream of praise kept me motivated throughout this thesis phase. I would also like to thank her post-doc Dr. Lucas Collodel for providing the relevant data files in an understandable manner, and providing the script to find mass and angular momentum of a given solution. Dr. Galin Gyulchev's insights on how to make the black hole shadow with the right parametrization, and his individually generated results which helped me to debug my own code were extremely vital as well.

But most importantly, what made my masters degree experience memorable was the time spent with my dear friends Shrish, Marius, Carla, Christina and Bipul. I will cherish all of the memories we made in these two years.

Contents

1	Introduction	5
2	Theoretical Background	8
2.1	Schwarzschild and Kerr Solutions of General Relativity	8
2.2	General Tensor Multi-Scalar Theory of Gravity	9
2.3	Two-Scalar Field Theory of Gravity	10
3	Geodesics in Standard Spacetimes	14
3.1	Conserved Quantities	14
3.2	Schwarzschild Spacetime	16
3.2.1	The Radial Equation	16
3.2.2	Massive Particle Orbits	16
3.2.3	Photon Orbits	18
3.3	Kerr Spacetime	19
3.3.1	The Radial Equation	19
3.3.2	Photon Orbits	20
3.3.3	Massive Particle Orbits	21
4	Ray Tracing with Analytical Metrics	23
4.1	Runge Kutta Integrators and Adaptive Time Stepping	23
4.2	Recipe and Results in Schwarzschild Spacetime	25
4.3	Recipe and Results in Kerr Spacetime	28
4.4	Shadows of Schwarzschild and Kerr Black Holes	31
4.4.1	Local Orthonormal Basis and Recipe	31
4.4.2	Discussion of Results	32
5	Ray Tracing with Numerical Metrics	36
5.1	Bicubic Spline Interpolation	36
5.2	Recipe and Comparison with a Kerr Black Hole	39
6	Results for KBHSH	46
6.1	Modified Recipe for Ray Tracing	46
6.2	Comparison of Cloud Shadows with Kerr Counterparts	47
6.3	Chaotic Shadows and Future Work	51
7	Conclusion	56

Chapter 1

Introduction

Given an initial configuration of a particle, determining its behaviour at any other future point in time is probably one of the most fundamental problems in physics. Starting from classical mechanics and the now more recent quantum and relativistic theories, determining the evolution of a particle through time and space is a pivotal feature of a theory. This thesis work focuses on the motion of photons in extremely strong gravitational environments.

In environments where gravity is very strong, Einstein's Theory of General Relativity is required to explain physical phenomena. This century old theory has passed numerous solar system and extra-galactic tests. The four canonical tests included explaining 1) the precession of Mercury [22], 2) the Shapiro Time Delay in radar signals sent between celestial bodies [38] 3) deflection of light during solar eclipses [21] as a product of gravitational lensing and 4) gravitational redshift of light coming from the solar chromosphere. On the extra-galactic scale, neutron stars and black holes provide the best laboratory for testing the validity of General Relativity. The first rapidly-rotating neutron star, dubbed as a pulsar was accidentally discovered by Jocelyn Bell Burnell in 1967 [30], and a few years later in 1974, Russell Hulse and Joseph H. Taylor Jr. discovered the first binary pulsar system [14], whose orbital characteristics matched the theoretical predictions of General Relativity. More recently, the gravitational wave astronomy sector has proven successful in using interferometry techniques and extremely sensitive detectors, to measure small amplitudes in oscillation resulting from gravitational waves passing through Earth. The first ever gravitational wave signal was detected by the Laser Interferometer Gravitational-Wave Observatory (LIGO) in 2015 [1]. Since then numerous black hole binary mergers have been detected at an outstandingly healthy rate.

Out of all the numerous laboratories available for testing General Relativity and alternate theories of gravity, this thesis will focus mainly on imaging black holes, dark astrophysical objects which feast on anything that comes within their event horizon radius, including light. This characteristic keeps black holes hidden in darkness and makes them very difficult to image. For the longest time, all hopes of finding a black hole were pinned on analyzing the gas, debris and stars which moved close to a possible potential candidate. Pioneering work was performed by Gez et al., who analyzed the motion of stars close to the Milky Way's centre over decades [24] using data from the Keck telescope. They concluded that the central dark mass has a density which can only be achieved by a star's collapse into a black hole. This object, now known as SgrA*, is believed to be a supermassive black hole with a mass estimate of 4×10^6 solar masses.

More recently however, the undertaking by the Event Horizon Telescope (EHT) Collaboration made possible the task of imaging a black hole by combining telescopes of the Very Long Baseline Interferometry (VLBI) project. The central supermassive black hole in galaxy M87 was pictured by EHT [7] in 2019, and the result in Figure 1.1 makes apparent the lensed accretion disk. Just three years later in 2022, [8] the EHT Collaboration successfully used similar techniques to produce the image of SgrA*. With rapid advances which make black hole imaging possible, we are now in a position to compare raw results from telescopes to theoretical models. After all, black holes are a theoretical prediction of Einstein's General Relativity; there may very well be other unknown objects that appear dark and have their own accretion disk. This takes us into the exciting domain of modified gravity.

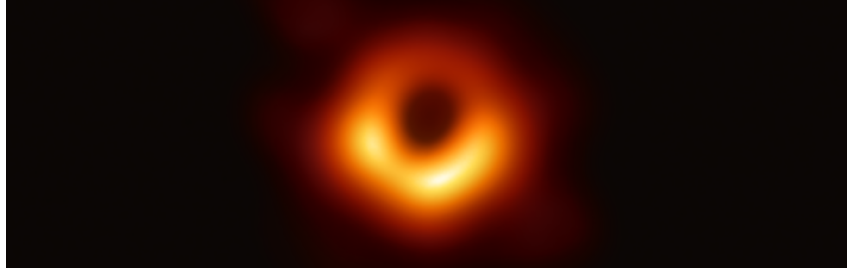


Figure 1.1: Image of the supermassive black hole $M87^*$ taken by the Event Horizon telescope and released in April 2019, see reference [7]. This billion solar mass compact object is found at the center of the galaxy $M87$, located 16 Mpc away from the Earth in the constellation of Virgo. The lensed accretion disk surrounds the photonsphere.

In Einstein's General Relativity, black holes are said to have no hair, with hair acting as a metaphor for a distinguishing feature. Given a mass, angular momentum and charge, one can completely describe a black hole; any two black holes with the same mass, angular momentum and charge are completely identical. This holds true even for a very large number of alternate gravity theories [29], [37]. In some scenarios however, it is possible to break this stringent notion [28], [4] and supply hair to the black hole in the form of scalar and tensor fields. Scalar fields appear regularly when considering perturbation in physics and modifications to a theory [28]. A noteworthy example is the Higgs boson in the standard model of particle physics, which is modelled as a scalar field. In many cases however, the existence of a scalar field renders black hole solutions unrealistic [9].

It was found more recently [31], [32], [3], [33] that black holes with synchronized hair can exist in the perturbative regime. The scalar fields in this scenario do not inherit the stationary and axisymmetric properties of the spacetime but instead have a harmonic dependence on t and ϕ . Stepping out of the perturbative regime, more interesting and novel non-linear solutions with synchronized hair were constructed in [27] and [26]. It is the tensor-multi-scalar theories (TMST) of gravity [15], [34] which allows for these kinds of solutions to exist. This class of theories is especially desirable because it produces well-posed solutions and models departure from General Relativity in the form of fields, a fundamental aspect in many theories. The Brans-Dicke Theory of gravity was the first such attempt at introducing one single scalar field coupled to gravity [15], and then Damour et al. developed the formalism to generalize this idea for N number of scalar fields. Continuous work within this field has lead to the prediction of some interesting objects such as solitonic, mixed soliton-fermion stars [39], [10], [18] and topological and scalarized neutron stars [20], [19].

One of the key historical methods to test General Relativity in the weak-field regime was the Parametrized Post-Newtonian (PPN) formalism. Damour et al. [15] developed the same approach for TMST gravity in the weak-field regime, and postulated binary neutron star systems as a laboratory for strong field experiments. With the recent advances in gravitational wave science, precise measurements of the signal could separate a pure Kerr black hole from modifications [5]. But as alluded to before, the vision of this work is to produce theoretical images that can serve as templates for the EHT Collaboration. Instead of modelling the accretion disk as was done in the theoretical modelling work of [7], the mission here is to capture the gravitationally lensed background as seen by an observer. The methodology implemented here is similar to the work performed by Lora et al. in [35] and also in [11], and [12]. Photons parametrized by the right initial conditions are shot backwards in time towards the compact object and their motion is allowed till they hit the horizon radius or escape to the computational celestial sphere. The celestial sphere here is divided into four quadrants, and the pixel from which the photon originated from on the observer's screen is assigned a colour according to which quadrant it intercepted (or black if it falls into the hole). This is the art of backward ray tracing, which involves solving the relevant equations of motion while keeping the Hamiltonian of every photon conserved.

The partitioning of this thesis is as follows: astrophysically significant solutions in standard General Relativity and the specific tensor-multi-scalar theory of gravity studied by Collodel et al. are discussed in Chapter 2. All these solutions admit special symmetries, so before directly integrating the geodesic equations, it is worth finding conserved quantities and re-casting the second order ordinary differential

equations into first order integrals of motion wherever possible. This is a more elegant and stable way of evolving a test particle in time, and is the focus of Chapter 3. Then, numerically implementing these analytical ideas is discussed in Chapter 4.

Finding solutions in TMST gravity is a herculean effort, and the general practice is to numerically solve the coupled set of partial differential equations. To generalize the recipe developed for ray tracing in Chapter 4 to numerical solutions, there is a need to continuously interpolate the TMST solutions for the equations of motion. For this task, bicubic spline interpolation is utilized and its implementation is discussed in depth in Chapter 5. Lastly in Chapter 6, the bicubic spline interpolation procedure is applied to the solutions found by Collodel et al, and shadows of Kerr Black Holes with Scalar Hair (KBHSH) are found.

One of the major undertakings of this thesis work was to develop C++ and python code from scratch. All the code can be found at this repository¹, and this thesis work can serve as its documentation.

¹<https://github.com/ayroy78/ray-tracing-geodesics-and-black-hole-shadows>

Chapter 2

Theoretical Background

Finding analytical or numerical solutions in Einstein Gravity and modified theories of gravity is an involved procedure. The goal of this chapter is to provide a brief overview of the Schwarzschild and Kerr solutions of Einstein Gravity and their significance. Then, the procedure of adding scalar fields to the theory is discussed, in the specific context of the work performed by Collodel et al. in [9].

2.1 Schwarzschild and Kerr Solutions of General Relativity

Space times in the Theory of General Relativity are described by a semi-Riemannian metric $g_{\mu\nu}$, which is the solution of the Einstein Equation given by,

$$Ric_{\mu\nu} - \frac{1}{2}g_{\mu\nu}R = \frac{8\pi G}{c^4}T_{\mu\nu}. \quad (2.1)$$

The left hand side contains curvature information stored in the Ricci Tensor $Ric_{\mu\nu}$, the metric $g_{\mu\nu}$ and the Ricci Scalar $R = Ric_{\mu\nu}g^{\mu\nu}$, where as the right hand side contains information about energy and matter in the form of the energy-momentum tensor $T_{\mu\nu}$. The Einstein Field Equation could also be viewed as the critical point of the following action,

$$S = \int \left(\frac{c^4}{16\pi G} R + S_M \right) \sqrt{-g} d^4x, \quad (2.2)$$

where S_M are arbitrary matter fields and g is the determinant of the metric. The tensor $T_{\mu\nu}$ then depends on the matter fields as,

$$T_{\mu\nu} = g_{\mu\nu}S_M - 2\frac{\delta S_M}{\delta g^{\mu\nu}}. \quad (2.3)$$

Equation (2.1) is a collection of sixteen coupled non-linear partial differential equations which are typically very difficult to solve for. The first non-trivial solution was provided by Karl Schwarzschild, and it describes a vacuum, spherically symmetric and static space time around an object of mass M . To begin deriving it, enforce the vacuum solution and set $T_{\mu\nu} = 0$ in the Einstein Equation to get,

$$Ric_{\mu\nu} - \frac{1}{2}g_{\mu\nu}R = 0 \implies R - 2R = 0 \implies R = 0 \implies Ric_{\mu\nu} = 0, \quad (2.4)$$

where the first implication comes by multiplication with the inverse metric and using $R = Ric_{ij}g^{ij}$ and $g_{ij}g^{jl} = \delta_i^l$. The third implication comes by resubstituting $R = 0$ in the Einstein Equation. So we solve for $Ric_{\mu\nu} = 0$ by starting with the ansatz,

$$ds^2 = A(r)dt^2 + B(r)dr^2 + r^2d\theta^2 + r^2\sin^2\theta d\phi^2. \quad (2.5)$$

For a Levi-Civita connection, the Christoffel Symbols are given in coordinate form as below

$$\Gamma_{ij}^k = \frac{1}{2}g^{lk} \left(\frac{\partial g_{il}}{\partial x^j} + \frac{\partial g_{jl}}{\partial x^i} - \frac{\partial g_{ij}}{\partial x^l} \right). \quad (2.6)$$

The ansatz of Equation 2.5 is then used to calculate the Christoffel Symbols using Equation 2.6, which are then substituted in the coordinate chart formula for the Ricci Tensor given by,

$$Ric_{\alpha\beta} = \frac{\partial\Gamma_{\alpha\beta}^\gamma}{\partial x^\gamma} - \frac{\partial\Gamma_{\alpha\gamma}^\gamma}{\partial x^\beta} + \Gamma_{\alpha\beta}^\gamma\Gamma_{\gamma\delta}^\delta - \Gamma_{\alpha\delta}^\gamma\Gamma_{\beta\gamma}^\delta. \quad (2.7)$$

Finally solving for $Ric_{\mu\nu} = 0$ under the application of appropriate boundary conditions, one then finds that the line element in $c = G = 1$ units in these Schwarzschild coordinates is equal to,

$$ds^2 = - \left(1 - \frac{2M}{r}\right) + \frac{1}{1 - \frac{2M}{r}} dr^2 + r^2(d\theta^2 + \sin^2\theta d\phi^2). \quad (2.8)$$

The singularity at $r = 2M$ is a coordinate singularity. While there are methods that allow connecting the regions $r < 2M$ and $r > 2M$ such as the Kruskal-Szekeres extension, these are avoided here, since the main goal of this work is to trace geodesics to create shadows detectable by cameras.

The Schwarzschild space time is excellent for modelling slowly-rotating black holes, but for rapidly rotating compact objects, one must drop the assumptions of spherical symmetry and staticity and seek an axisymmetrical and stationary solution. Such a solution was derived by Roy Kerr using creative and robust mathematical methods which are not discussed here. Only its final form in Boyer-Lindquist coordinates is presented here in Equation 2.9.

$$ds^2 = - \left(1 - \frac{r_s r}{\Sigma}\right) dt^2 - \frac{2r_s r a \sin^2\theta}{\Sigma} dt d\phi + \frac{\Sigma}{\Delta} dr^2 + \Sigma d\theta^2 + \left(r^2 + a^2 + \frac{r_s r a^2 \sin^2\theta}{\Sigma}\right) \sin^2\theta d\phi^2, \quad (2.9)$$

where a is the angular momentum per unit mass of the rotating black hole and $r_s = 2M$ is the corresponding Schwarzschild radius. The definitions for Σ and Δ are as follows,

$$\Sigma = r^2 + a^2 \cos^2\theta, \quad (2.10)$$

$$\Delta = r^2 + a^2 - 2Mr. \quad (2.11)$$

Under the condition that $a = 0$, Equation (2.9) reduces to the Schwarzschild line element in Equation (2.8). The change from a static and spherically symmetric space time to a stationary and axisymmetric one introduces an off-diagonal term which modifies the equations of motion considerably as is discussed in Chapter 3. Looking at the metric in Equation (2.9), singularities occur at the following,

$$\Delta = 0 \implies r_{\pm} = M \pm \sqrt{M^2 - a^2}, \quad (2.12)$$

$$\Sigma = 0 \implies r = 0 \quad \text{and} \quad \theta = \pi/2. \quad (2.13)$$

Just like in the Schwarzschild case, the discussion and treatment is limited to the outer event horizon, r_+ , because the main goal is to track geodesics till they are visible to a camera. It should also be noted that physically valid choices of a are such that $|a| < M$, the so-called sub-extremal case which avoids naked singularities and preserves the black hole thermodynamic laws.

2.2 General Tensor Multi-Scalar Theory of Gravity

Scalar fields are added to the theory of gravity by modifying the Einstein-Hilbert action in Equation 2.2. The earliest notable attempt was the Brans-Dicke Theory [15], which works with the action [23] (using $c = G = 1$),

$$S = \frac{1}{16\pi} \int \left(\varphi R - \frac{\omega}{\varphi} \partial_a \varphi \partial^a \varphi + S_M \right) \sqrt{-g} d^4x, \quad (2.14)$$

where now φ is the scalar field and ω is the dimensionless Dicke coupling constant. The field equations found by varying the action with respect to the metric and the scalar field are given by,

$$G_{ab} = \frac{8\pi}{\varphi} T_{ab} + \frac{\omega}{\varphi^2} \left(\partial_a \varphi \partial_b \varphi - \frac{1}{2} g_{ab} \partial_c \varphi \partial^c \varphi \right) + \frac{1}{\varphi} (\nabla_a \nabla_b \varphi - g_{ab} \square \varphi), \quad (2.15)$$

$$\square \varphi = \frac{8\pi}{3+2\omega} T, \quad (2.16)$$

where now T is the trace of the energy-momentum tensor T_{ab} , and \square is the covariant wave operator. The Brans-Dicke Theory of gravity fails to be convincing, because of the presence of only one tunable parameter ω , and all its predictions differing from General Relativistic quantities by the order of $\frac{1}{\omega}$ in both strong and weak field regimes [15]. On the other hand, the general class of tensor multi-scalar theories predicts values which agree under the weak field regime, but deviate in strong gravitational

environments which differentiates it from General Relativity. The general structure of these theories is presented over here, following the formalism outlined in [15] and in [34]. The action is of the form (with $c = 1$),

$$S = \frac{1}{4\pi G} \int \sqrt{-g} \left(\frac{R}{4} - \frac{1}{2} g^{\mu\nu} \gamma_{ab}(\varphi) \partial_\mu \varphi^a \partial_\nu \varphi^b - V(\varphi) \right) d^4x + S_M [A^2(\varphi) g_{\mu\nu}; \Psi], \quad (2.17)$$

where γ_{ab} is the metric for the N number of scalar fields that live on the target space manifold, $V(\varphi)$ is the potential associated to the fields and A is the conformal factor relating the Einstein-frame metric $g_{\mu\nu}$ to the Jordan-frame metric $\tilde{g}_{\mu\nu} = A^2(\varphi) g_{\mu\nu}$. Both the frames are equivalent ways of looking at the theory, with the Einstein frame coming historically first as the Theory of General Relativity came before TMST theories of gravity. The Jordan-frame metric is sometimes also called the physical metric, because it captures the properties of the scalar fields which play a role in physically describing the spacetime.

The structure of Equation (2.17) is fairly intuitive; it can be decomposed as $S = S_{EH} + S_\varphi + S_M$. To the Einstein-Hilbert action S_{EH} , additional degrees of freedom are added via a contribution from the fields in the form of S_φ , where as matter sources represented by S_M are written outside the main integral. S_φ has a kinetic energy term and a potential term, so it poses as an additional degree of freedom that would satisfy a Klein-Gordon like expression. The magnitude of the velocity of the fields is calculated using the metric $\gamma_{ab}(\varphi)$, signifying that the fields live on a manifold with its own metric. As a consequence of S_M being outside the main integral, it can be completely described by the Jordan-frame metric. It is still any general functional, as is shown below for the case for a spin-0 massive matter field [15].

$$S_M = -\frac{1}{2} \int \frac{d^4x}{c} \sqrt{\tilde{g}} \left(\tilde{g}^{\mu\nu} \partial_\mu \psi \partial_\nu \psi + \frac{\tilde{m}^2 \psi^2 c^2}{\hbar^2} \right). \quad (2.18)$$

The field equations which come from varying the action with respect to the metric $g_{\mu\nu}$ and the N number of scalar fields φ are,

$$R_{\mu\nu} = 2\gamma_{ab}(\varphi) \nabla_\mu \varphi^a \nabla_\nu \varphi^b + 2V(\varphi) g_{\mu\nu} + 8\pi G \left(T_{\mu\nu} - \frac{1}{2} T g_{\mu\nu} \right), \quad (2.19)$$

$$\square \varphi^a = -\gamma_{bc}^a(\varphi) g^{\mu\nu} \nabla_\mu \varphi^b \nabla_\nu \varphi^c + \gamma^{ab}(\varphi) \frac{\partial V(\varphi)}{\partial \varphi^b} - 4\pi G \gamma^{ab}(\varphi) \frac{\partial \log A(\varphi)}{\partial \varphi^b} T, \quad (2.20)$$

where γ_{bc}^a are the Christoffel symbols of the target space manifold endowed with the metric γ_{ab} . Equation (2.20) is also sometimes referred to as the Klein-Gordon-Einstein (KGE) equation. The energy-momentum tensor is now given by,

$$T_{\mu\nu} = -\frac{2}{\sqrt{-g}} \frac{\delta S_M (A^2(\varphi) g_{\rho\sigma}; \Psi)}{\delta g^{\mu\nu}}. \quad (2.21)$$

2.3 Two-Scalar Field Theory of Gravity

We now shift our attention to the specific solutions whose shadows we would like to create. Modified theory of gravity with two scalar fields is discussed here, closely following the work in [9] by Collodel et al. This is a special case of the general tensor multi-scalar theory discussed above, with $N = 2$. In this framework, the governing action is given exactly by Equation (2.17), where now $a, b = 1/2$, i.e. the scalar field terms have two indices. We seek vacuum solutions that mimic black holes and self-gravitating objects, so $\Psi = 0$. It should be noted that $A(\varphi)$ might still be needed if a conversion to the Jordan frame is required, which as stated before is an equivalent frame for doing calculations but is deemed more physical because of containing information about matter coupling.

Varying the expression appearing in Equation (2.17) again leads to a system of coupled partial differential equations for the metric $g_{\mu\nu}$ and the fields φ . Explicitly, with $S_M = 0$, the equations read as,

$$T_{\mu\nu} = 0, \quad (2.22)$$

$$R_{\mu\nu} = 2\gamma_{ab} \partial_\mu \varphi^a \partial_\nu \varphi^b + 2V(\varphi) g_{\mu\nu}, \quad (2.23)$$

$$\square \varphi^a = -\gamma_{bc}^a(\varphi) g^{\mu\nu} \partial_\mu \varphi^b \partial_\nu \varphi^c + \gamma^{ab}(\varphi) \frac{\partial V(\varphi)}{\partial \varphi^b}. \quad (2.24)$$

To solve Equations (2.23) and (2.24), added structure was supplied. The metric of the target space manifold $\gamma_{ab}(\varphi)$ is written in a conformally flat form,

$$\gamma_{ab} = \Omega^2(\varphi)\delta_{ab}, \quad (2.25)$$

where δ_{ab} is the usual Kronecker Delta. The conformal factor Ω is given by,

$$\Omega^2 = \frac{1}{\left(1 + \frac{\kappa}{4}\delta_{ab}\varphi^a\varphi^b\right)^2}, \quad (2.26)$$

and κ is the Gaussian curvature of the manifold consisting of the scalar fields. The conformal factor is a function of the combination of the fields given as $\psi^2 = \delta_{ab}\varphi^a\varphi^b$, and the same follows for the potential given as

$$V(\psi) = \frac{1}{2}\mu^2\psi^2. \quad (2.27)$$

For simplicity, the conformal factor between the Einstein and Jordan frames given by $A(\varphi)$ is written as,

$$A(\psi) = \exp\left(\frac{1}{2}\beta\psi^2\right). \quad (2.28)$$

Since we are interested in rotating black holes and black hole mimickers, the ansatz for the stationary and axisymmetric line element is chosen to be,

$$ds^2 = -\mathcal{N}e^{2F_0}dt^2 + e^{2F_1}\left(\frac{dr^2}{\mathcal{N}} + r^2d\theta^2\right) + e^{2F_2}r^2\sin^2\theta\left(d\phi - \frac{\omega}{r}dt\right)^2, \quad (2.29)$$

where $\mathcal{N} = 1 - \frac{r_H}{r}$, and r_H is the location of the horizon in these coordinates. Writing out the line element in a form comparable with Kerr in Boyer-Lindquist coordinates as in Equation (2.9) yields

$$ds^2 = (-\mathcal{N}e^{2F_0} + e^{2F_2}\omega^2\sin^2\theta)dt^2 - 2e^{2F_2}r\omega\sin^2\theta dtd\phi + \frac{e^{2F_1}}{\mathcal{N}}dr^2 + e^{2F_1}r^2d\theta^2 + e^{2F_2}r^2\sin^2\theta d\phi^2, \quad (2.30)$$

and is observed to have the same number of components as in Equation (2.9). In fact, for Kerr black holes, there exists an isometry between these two metrics under the mapping as given in [26],

$$r = R - \frac{a^2}{R_H}, \quad (2.31)$$

where r is the radial coordinate in Equation (2.30) and R is the Boyer-Lindquist radial coordinate appearing as lower case r in Equation (2.9). R_H is now the outer event horizon called as r_+ before. The relevant terms appearing in Equation (2.30) must then obey the following,

$$e^{2F_1} = \left(1 - \frac{c_t}{r}\right)^2 + c_t(c_t - r_H)\frac{\cos^2\theta}{r^2}, \quad (2.32)$$

$$e^{2F_2} = e^{-2F_1} \left(\left(\left(1 - \frac{c_t}{r}\right)^2 + \frac{c_t(c_t - r_H)}{r^2}\right)^2 + c_t(r_H - c_t)\left(1 - \frac{r_H}{r}\right)\frac{\sin^2\theta}{r^2} \right), \quad (2.33)$$

$$F_0 = -F_2, \quad \omega = e^{-2(F_1+F_2)}\sqrt{c_t(c_t - r_H)}(r_H - 2c_t)\frac{(1 - \frac{c_t}{r})}{r^2}, \quad (2.34)$$

and r_H and c_t are related to M and J as follows,

$$M = \frac{1}{2}(r_H - 2c_t), \quad J = \frac{1}{2}\sqrt{c_t(c_t - r_H)}(r_H - 2c_t). \quad (2.35)$$

As expected, isolating for r_H gives what one expects from the mapping in Equation (2.31), i.e, $r_H = R_H - \frac{a^2}{R_H}$.

Under the framework of scalar-field gravity however, solutions described by Equation (2.30) can't be interpreted as Kerr black holes and relation 2.31 does not hold because of the presence of non-zero scalar fields. The ansatz used for the fields is as follows,

$$\varphi^1 = \psi(r, \theta)\cos(\omega_s t + m\phi), \quad \varphi^2 = \psi(r, \theta)\sin(\omega_s t + m\phi), \quad (2.36)$$

showcasing that there is really only one fundamental field ψ and φ^1 can be rotated to φ^2 via $U(1)$ symmetry. Hence the goal is to simultaneously solve for the field magnitude ψ and the quantities (F_0, F_1, F_2, ω) appearing in the ansatz in Equation (2.30) subject to the following boundary conditions. To express these conditions, we can define a compactified radial coordinate $x \in [0, 1]$ as follows,

$$\bar{r} = \sqrt{r^2 - r_H^2}, \quad x = \frac{\bar{r}}{\bar{r} + 1}, \quad (2.37)$$

and it is easy to check that $x(r = r_H) = 0$ and $x(r = \infty) = 1$. Using this we can say,

$$\partial_x F_0|_{x=0} = 0, \quad \partial_x F_1|_{x=0} = 0, \quad \partial_x F_2|_{x=0} = 0, \quad \partial_x \psi|_{x=0} = 0, \quad \omega|_{x=0} = -\frac{r_H \omega_s}{m}. \quad (2.38)$$

The first four are just the Neumann boundary conditions at the horizon, and the condition on ω comes from imposing regularity. Next, asymptotic flatness requires that,

$$F_0|_{x=1} = 0, \quad F_1|_{x=1} = 0, \quad F_2|_{x=1} = 0, \quad \omega|_{x=1} = 0, \quad \psi|_{x=1} = 0. \quad (2.39)$$

The asymptotic behaviour of ψ is described by,

$$\lim_{r \rightarrow \infty} \psi \propto \frac{1}{r} \exp\left(-\sqrt{\mu^2 - \omega_s^2} r\right), \quad (2.40)$$

thereby bounding ω_s via $\omega_s^2 \leq \mu^2$. The corresponding conditions for behaviour with respect to the polar angle are as follows,

$$\partial_\theta F_0|_{\theta=0} = 0, \quad \partial_\theta F_1|_{\theta=0} = 0, \quad \partial_\theta F_2|_{\theta=0} = 0, \quad \partial_\theta \omega|_{\theta=0} = 0, \quad \psi|_{\theta=0} = 0, \quad (2.41)$$

$$\partial_\theta F_0|_{\theta=\pi/2} = 0, \quad \partial_\theta F_1|_{\theta=\pi/2} = 0, \quad \partial_\theta F_2|_{\theta=\pi/2} = 0, \quad \partial_\theta \omega|_{\theta=\pi/2} = 0, \quad \partial_\theta \psi|_{\theta=\pi/2} = 0, \quad (2.42)$$

where the first line of conditions comes from regularity and axisymmetry, and the second line comes from reflection symmetry about the equatorial plane. The ADM mass and angular momentum can be found asymptotically as follows,

$$M = \frac{1}{2} \lim_{r \rightarrow \infty} r^2 \partial_r F_0, \quad J = \frac{1}{2} \lim_{r \rightarrow \infty} r^2 \omega. \quad (2.43)$$

The ADM mass and angular momentum have varying contributions from the hole and the hair. To specify the hairiness, the normalized charge q defined according to [27] as $q = \frac{mQ}{J}$ is used, where Q is the conserved Noether Charge. Interestingly, the angular momentum of the scalar field is quantized in terms of the Noether Charge Q , i.e. $J_\psi = mQ$, so we simply have $q = \frac{J_\psi}{J}$. Thus $q = 0$ solutions are completely Kerr-like, and are called as clouds, where as $q = 1$ solutions are completely hair-dominated.

The formal PDE problem was solved numerically for Gaussian curvatures $\kappa \in (-5, -1, 0, 1, 5)$, fixing $m = 1$ and $\beta = -6$ by Collodel et al. Solutions were plotted as tracks of r_H in the $M - \omega_s$ plane, both axes normalized by the scalar field mass μ . Figure 2.1 shows the plot for the cases $\kappa = 0, -5, 5$. For all the plots, the black line marks the extremal Kerr limit, with $a = M$ and everything below this line belongs to the Kerr class of solutions. The yellow region consists of KBHSH solutions, which has a boundary subdivided into solitonic, extremal hairy black hole and cloud solutions. Both solitons and extremal hairy black holes have vanishing horizon radius ($r_H = 0$), but solitonic solutions marked with a red line additionally have a normalized charge $q = 1$. Cloud solutions marked with a blue line have $q = 0$ and are qualitatively similar to Kerr black holes.

It is observed that the solution space has turning points. If we follow the red solitonic curve, the first turning point occurs at the minimum value of ω_s , with negative gaussian curvatures having a lower ω_s value at the turning point. The allowed ω_s values continue to grow till the solution space winds on itself in the so called inspiralling region, and was observed to be a numerically challenging. As can be seen in Figure 2.1b, convergence was halted well before the second turning point. Solutions with a positive gaussian curvature have a smaller ω_s value at this second turning point, with a greater total mass M . Traversing outside the inspiralling region, the solitons meet extremal hairy black holes with steadily decreasing charge q till they meet the cloud solutions marked in blue, which have $q = 0$.

From the point of view of r_h , smaller values of r_h have a larger domain of existence in ω_s , because these move closer to the solitonic and external black hole limit, both of which have a vanishing horizon

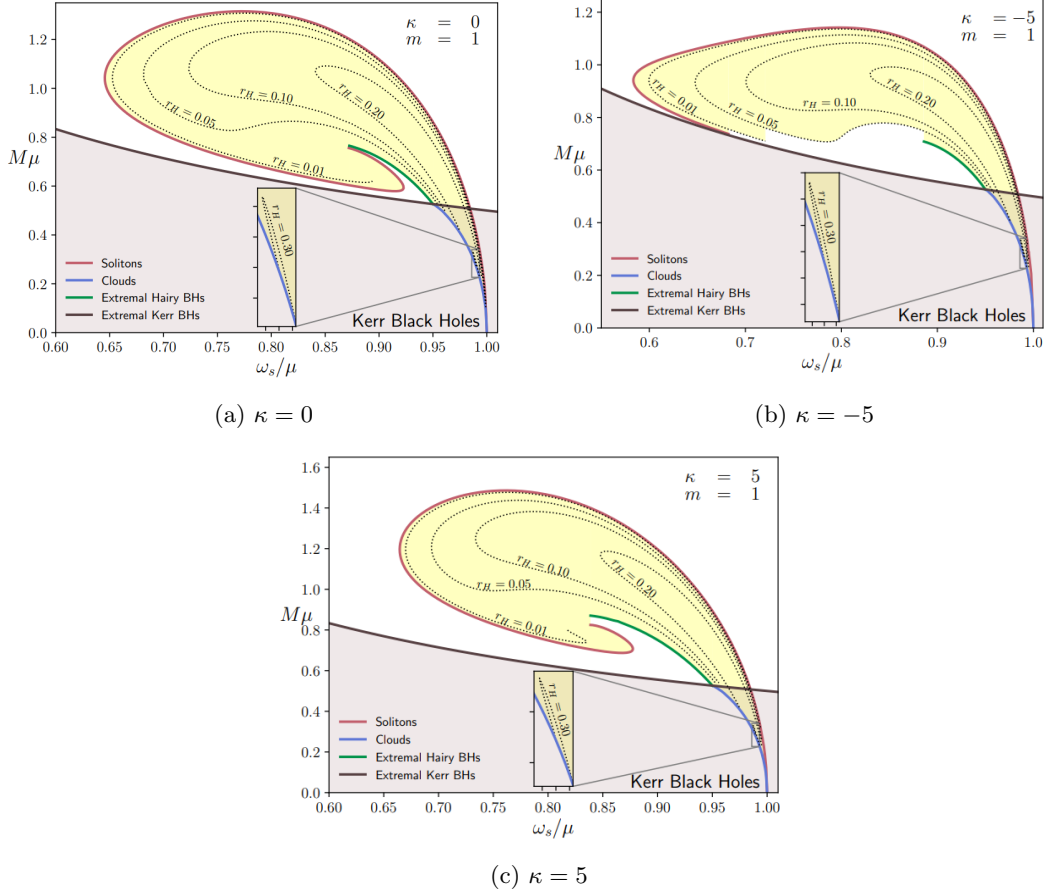


Figure 2.1: Tracks for fixed r_H in the $M - \omega_s$ plane, taken from [9] for $\kappa = 0, -5, 5$. The solutions are obtained by solving a coupled set of partial differential equations found by varying the Einstein-Hilbert action coupled to two scalar fields. The black line and below holds Kerr solutions, whereas new exotic solutions are held in the yellow bubble. It is bounded by three classes of solutions, solitonic, extremal hairy black hole and cloud solutions, depending on the value of r_H and normalized charge $q = \frac{mQ}{J}$, as explained in the text.

radius. Tracks denoted with an extremely small value of r_h start and stop at the cloud line. More generally however, each fixed track of r_h starts at the Minkowski limit with $\omega_s/\mu = 1$ and stops at the cloud line.

In all the plots of Figure 2.1, the red solitonic line and the green extremal hairy black hole line show discernible differences, but the blue cloud line tends to stay similar. This is because small differences in κ result in only small perturbations to the theory when the scalar fields are infinitesimally small on a Kerr background. To see a marked difference a much higher value of κ is required, and this was verified using $\kappa = 100$.

Chapter 3

Geodesics in Standard Spacetimes

The goal of this thesis is to trace photon trajectories for the KBHSH solutions discussed in Chapter 2 to make a shadow. Since in some way, these solutions are modifications of standard spacetimes studied in General Relativity, it is worth reviewing the basics of geodesic motion in Schwarzschild and Kerr spacetime. The brute force approach to capture the motion of test particles is to employ the geodesic equation, given by,

$$\frac{d^2x^k}{d\tau^2} = -\Gamma_{ij}^k \frac{dx^i}{d\tau} \frac{dx^j}{d\tau}, \quad (3.1)$$

where $k = 0, 1, 2, 3$ stands for spacetime indices, x is the spacetime coordinate, τ is an affine parameter, and Γ_{ij}^k is the placeholder for the Christoffel Symbols. The method developed here takes a different and more elegant approach, one which involves seeking out conserved quantities that introduce first order integrals of motion. These are not only easier to solve on the computer, but also introduce constant quantities in the numerical scheme which increases stability. General particle and photon orbits are discussed for Schwarzschild space time where as the discussion is limited to specific orbits in Kerr space time to demonstrate its noteworthy features.

3.1 Conserved Quantities

Integral flows and the Lie Derivative are required to understand the constants of motion along a geodesic; the formalism developed here is derived from [17]. The integral flow of a vector field X is a map $\Phi(s)$ given as,

$$\dot{\Phi}(s) = X_{\Phi(s)}, \quad (3.2)$$

which has a solution given an initial condition $\Phi_0 = \Phi(s = 0)$.

Next, the Lie derivative of a tensor field T in the direction of a vector Y is given as

$$\mathcal{L}_Y T = \frac{d}{ds}|_{s=0} \Phi^* T, \quad (3.3)$$

where Φ is a flow map of Y given by Equation (3.2). Restricting $T = g$, the metric tensor, a Killing vector Y is defined such that

$$\mathcal{L}_Y g = 0, \quad (3.4)$$

that is, the Lie Derivative is zero.

Next, we define the standard Gauss basis vectors in the t and ϕ directions as,

$$\partial_t = \begin{pmatrix} 1 \\ 0 \\ 0 \\ 0 \end{pmatrix}, \quad \partial_\phi = \begin{pmatrix} 0 \\ 0 \\ 0 \\ 1 \end{pmatrix}. \quad (3.5)$$

The corresponding flow maps of ∂_t and ∂_ϕ are trivial to solve using Equation (3.2) and are simply given by,

$$\Phi_{\partial_t} = \begin{pmatrix} s \\ 0 \\ 0 \\ 0 \end{pmatrix}, \quad \Phi_{\partial_\phi} = \begin{pmatrix} 0 \\ 0 \\ 0 \\ s \end{pmatrix}. \quad (3.6)$$

Next we calculate the Lie Derivative of the Schwarzschild and Kerr metrics in the direction of ∂_t and ∂_ϕ and show that these are Killing vector fields. Recalling that the Schwarzschild line element given in Equation (2.8) is independent off t and ϕ , the pullback of the metric along either of these flow maps preserves the metric, $\Phi^*g = g$, that is, these flow maps are isometries. Carrying out the calculation, we get,

$$\mathcal{L}_Y g = \frac{d}{ds}|_{s=0} \Phi^* g = \frac{d}{ds}|_{s=0} g = 0, \quad \mathcal{Y} = \partial_t / \partial_\phi. \quad (3.7)$$

Next we derive the Killing Equation as follows. An arbitrary Killing vector is labelled as X and its behaviour with two test vectors Y and Z is calculated. Starting with the knowledge that the Lie Derivative satisfies the product rule in the second slot we get

$$\mathcal{L}_X(g(Y, Z)) = (\mathcal{L}_X g)(Y, Z) + g(\mathcal{L}_X Y, Z) + g(\mathcal{L}_X Z, Y). \quad (3.8)$$

Now we use the following facts about the Lie Derivative and the Killing vector X ,

$$\mathcal{L}_X(g(Y, Z)) = X(g(Y, Z)), \quad \mathcal{L}_X g = 0, \quad \mathcal{L}_X Y = [X, Y], \quad (3.9)$$

where the first equality means that the Lie Derivative is the directional derivative on functions, the second is the definition of a Killing vector field, and the third is the Lie Derivative of two vector fields. The expression now becomes

$$X(g(Y, Z)) = g([X, Y], Z) + g([X, Z], Y). \quad (3.10)$$

Now we use metric compatibility on the left and torsion free property on the right to introduce the Levi-Civita connection as follows,

$$\cancel{g(\nabla_X Y, Z)} + \cancel{g(Y, \nabla_X Z)} = g(\nabla_X Y - \nabla_Y X, Z) + g(\nabla_X Z - \nabla_Z X, Y), \quad (3.11)$$

$$0 = g(-\nabla_Y X, Z) + g(-\nabla_Z X, Y). \quad (3.12)$$

Then the Killing Equation in desired form is

$$g(\nabla_Y X, Z) = -g(\nabla_Z X, Y). \quad (3.13)$$

If we set $Y = Z = \dot{\gamma}$ in the Killing Equation, we then have

$$g(\nabla_{\dot{\gamma}} X, \dot{\gamma}) = -g(\nabla_{\dot{\gamma}} X, \dot{\gamma}) \implies g(\nabla_{\dot{\gamma}} X, \dot{\gamma}) = 0. \quad (3.14)$$

Now to show that a quantity $\kappa := g(\dot{\gamma}, X)$ is constant along a geodesic γ , take its derivative,

$$\nabla_{\dot{\gamma}} \kappa = d\kappa(\dot{\gamma}) = g(\nabla_{\dot{\gamma}} \dot{\gamma}, X) + g(\dot{\gamma}, \nabla_{\dot{\gamma}} X). \quad (3.15)$$

Now because γ is a geodesic of a freely falling particle, we have that $\nabla_{\dot{\gamma}} \dot{\gamma} = 0$ and the first term is equal to zero. From Equation (3.14), the second term is also zero. So

$$\nabla_{\dot{\gamma}} \kappa = 0 \implies g(\dot{\gamma}, X) = \text{const.} \quad (3.16)$$

So we have shown that each Killing vector X yields a conserved quantity along the geodesic, labelled as κ , up to a sign.

Recalling Noether's Theorem, each such conserved quantity along the geodesic corresponds to a symmetry, which in this case is an isometry map for the metric. The symmetry maps are associated to time and rotation, meaning that the conserved quantities correspond to energy and angular momentum respectively. In the next sections we will define these constants and derive the equations of motion invoking these conserved quantities.

3.2 Schwarzschild Spacetime

3.2.1 The Radial Equation

The discussion here about Schwarzschild spacetime follows the development in [25]. The Schwarzschild line element is repeated below for convenience,

$$ds^2 = - \left(1 - \frac{2M}{r}\right) dt^2 + \frac{1}{1 - \frac{2M}{r}} dr^2 + r^2(d\theta^2 + \sin^2\theta d\phi^2), \quad (3.17)$$

and it models the spacetime surrounding a spherically symmetric and static star or blackhole. Using the work of the previous section, the conserved energy and angular momentum are given by

$$e := -g_{ij}(\partial_t)^i(\dot{\gamma})^j = \left(1 - \frac{2M}{r}\right) \frac{dt}{d\tau}, \quad (3.18)$$

$$l := g_{ij}(\partial_\phi)^i(\dot{\gamma})^j = r^2 \sin^2\theta \frac{d\phi}{d\tau} = r^2 \frac{d\phi}{d\tau}, \quad \theta = \frac{\pi}{2}, \quad (3.19)$$

where in the last expression one can fix the plane of the particle at the equator. Now starting with the normalization condition of four-velocity, we derive the radial equation of motion as follows

$$g(\dot{\gamma}, \dot{\gamma}) = \mu, \quad (3.20)$$

where $\mu = 0$ for null geodesics and $\mu = -1$ for massive particles.

$$-\left(1 - \frac{2M}{r}\right) t^2 + \frac{1}{\left(1 - \frac{2M}{r}\right)} \dot{r}^2 + r^2 \dot{\phi}^2 = \mu. \quad (3.21)$$

Then using the definitions of Equations (3.18) and (3.19) we get

$$\frac{e^2}{\left(1 - \frac{2M}{r}\right)} - \frac{1}{\left(1 - \frac{2M}{r}\right)} \dot{r}^2 - \frac{l^2}{r^2} = -\mu, \quad (3.22)$$

$$e^2 - \dot{r}^2 - \left(1 - \frac{2M}{r}\right) \frac{l^2}{r^2} = -\mu \left(1 - \frac{2M}{r}\right), \quad (3.23)$$

$$e^2 + \mu = \dot{r}^2 + \frac{l^2}{r^2} - \frac{2Ml^2}{r^3} + \frac{2M\mu}{r}, \quad (3.24)$$

$$\frac{e^2 + \mu}{2} = \frac{1}{2} \dot{r}^2 + \frac{l^2}{2r^2} + \frac{M\mu}{r} - \frac{Ml^2}{r^3}. \quad (3.25)$$

Setting $\mu = 0$ for photons we get

$$H := \frac{e^2}{2} = \frac{1}{2} \dot{r}^2 + \frac{l^2}{2r^2} - \frac{Ml^2}{r^3}, \quad (3.26)$$

and setting $\mu = -1$ for massive particles we get

$$H := \frac{e^2 - 1}{2} = \frac{1}{2} \dot{r}^2 + \frac{l^2}{2r^2} - \frac{M}{r} - \frac{Ml^2}{r^3}. \quad (3.27)$$

Equations (3.26) and (3.27) govern the motion of photons and point mass particles in Schwarzschild spacetime. The radial equations are very similar to the Newtonian case, except for the appearance of the $-\frac{Ml^2}{r^3}$ term that acts as an attractive term, overpowering the centrifugal barrier. We will call the above expressions the Hamiltonian of the system and denote them by H .

3.2.2 Massive Particle Orbits

The deduced effective potential for massive particles is equal to

$$V_{eff}(l, r, M) := \frac{l^2}{2r^2} - \frac{M}{r} - \frac{Ml^2}{r^3}. \quad (3.28)$$

Plotting the effective potential given e, l readily provides us information about what kind of trajectory the particle can perform. We start by discussing circular orbits which appear at the extrema of the effective potential. These are found using taking the first derivative of the effective potential and setting to zero. Doing so gives that

$$0 = \frac{dV_{eff}}{dr} = -\frac{l^2}{r^3} + \frac{M}{r^2} + \frac{3Ml^2}{r^4}, \quad (3.29)$$

$$0 = Mr^2 - l^2r + 3Ml^2. \quad (3.30)$$

Solving for the angular momentum of a circular orbit gives that

$$l_{circ}^2 = \frac{Mr^2}{r - 3M}, \implies r_{circ} > 3M. \quad (3.31)$$

Using this and the fact that $\dot{r} = 0$ for circular orbits in Equation (3.27) gives the Hamiltonian of a massive particle in circular orbit,

$$H_{circ} = \frac{e^2 - 1}{2}_{circ} = \frac{4M^2 - Mr}{2(r - 3M)r}. \quad (3.32)$$

Solving for r directly using the quadratic formula gives us that

$$r_{circ} = \frac{l^2}{2M} \pm \sqrt{\frac{l^4 - 12M^2l^2}{4M^2}}, \quad (3.33)$$

$$r_{circ} = \frac{l^2}{2M} \left(1 \pm \sqrt{1 - \frac{12M^2}{l^2}} \right), \quad (3.34)$$

which tells that circular orbits for massive particles occur only when

$$l \geq l_{crit} = \sqrt{12}M, \quad (3.35)$$

meaning that maxima and minima of the potential occur only when the angular momentum exceeds or equals this critical value. The radius of the circular orbit at the critical value of angular momentum is

$$r_{ISCO} = \frac{12M^2}{2M} = 6M = 3R_s, \quad (3.36)$$

and is called the innermost stable circular orbit, because for $l > l_{crit}$ all stable circular orbits are larger than $3R_s$. Lastly, it remains to show that Kepler's Law holds for circular orbits. Start by writing the angular velocity as

$$\Omega = \frac{d\phi}{dt} = \frac{\frac{d\phi}{d\tau}}{\frac{dt}{d\tau}} = \frac{l}{e} \left(\frac{1}{r} \right)^2 \left(1 - \frac{2M}{r} \right), \quad (3.37)$$

and the expression for $\frac{l}{e}$ is found using Equation (3.27) for $\dot{r} = 0$. It gives

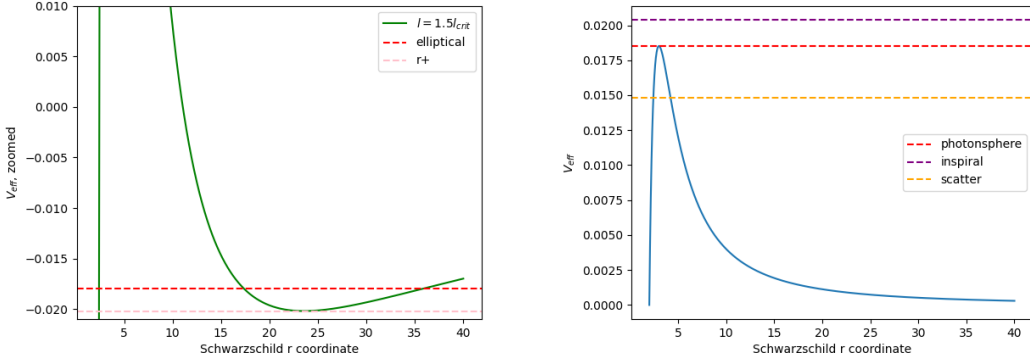
$$\frac{e}{l} = \left(1 - \frac{2M}{r} \right)^{\frac{1}{2}} \frac{1}{r} \left(1 + \frac{r^2}{l^2} \right)^{\frac{1}{2}}. \quad (3.38)$$

Using the expression for l_{circ} then gives the result,

$$\Omega^2 r^3 = M, \quad (3.39)$$

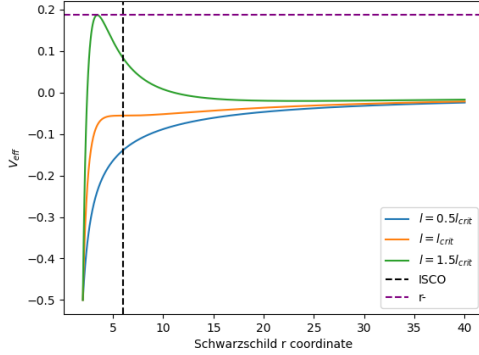
that Kepler's Law holds for massive circular orbits in Schwarzschild space time. The stability of these circular orbits and other qualitative features of massive particle orbits is observable by plotting the potential in Equation (3.28), displayed in Figure (3.1).

If e is chosen in such a way that the Hamiltonian of Equation (3.27) equals the maxima and minima of the potential in Equation (3.28), then the particle is confined to stay there forever for stable circular orbits. In the case of the unstable circular orbit, the particle has freedom to arrive from infinity or start on an outward-bound journey and be captured into a circular orbit. If the particle has more energy than the maxima of the effective potential, it will inspiral if it comes in from infinity, or escape to infinity if it is directed outwards. Lastly, elliptical orbits are the other class of bound orbits apart from circular orbits, and occur at a specific range of e values. Elliptical orbits show the interesting property of precession of their perihelion and is numerically re-created in Chapter 4, when ray tracing is discussed.



(a) Zoomed V_{eff} for massive particles in $M = 1$ Schwarzschild spacetime.

(b) V_{eff} for photons with $l = 1$ in $M = 1$ Schwarzschild spacetime.



(c) V_{eff} for massive particles in $M = 1$ Schwarzschild spacetime.

Figure 3.1: The figures show the effective potential for massive and massless particles respectively, in Schwarzschild spacetime for $M = 1$. From 3.1c, we see that for $l < l_{crit}$ only permits inspiral orbits, where as for $l \geq l_{crit}$ interesting geometric orbits are observable. 3.1a zooms into the interesting region of the $l = 1.5l_{crit}$ orbit, with the red line corresponding to an orbit with elliptic shape and the pink line corresponding to the stable circular orbit. The purple line in 3.1c corresponds to the unstable circular orbit. The red line 3.1b marks the photon sphere orbit, the orange line below is a scatter orbit for a photon directed from infinity, where as the purple line marks an inspiral photon.

3.2.3 Photon Orbits

The same procedure from the last section is followed, and first the effective potential is defined as

$$V_{eff}(l, r, M) := \frac{l^2}{2r^2} - \frac{Ml^2}{r^3}. \quad (3.40)$$

Locating circular orbits as before yields

$$0 = \frac{dV_{eff}}{dr} = -\frac{l^2}{r^3} + \frac{3Ml^2}{r^4} \implies r_{circ} = 3M. \quad (3.41)$$

We see that unlike the massive particle case, there exists a circular photon orbit for any choice of angular momentum parameter l . The Hamiltonian appearing in Equation (3.26) for circular orbits is then equal to

$$H_{circ} = \frac{e^2}{2_{circ}} = \frac{l^2}{54M^2}. \quad (3.42)$$

Photons that orbit a Schwarzschild black hole in a circular trajectory at $r = 3M$ are trapped into the photon sphere. These orbits are unstable, as can be verified by the plot displayed in Figure 3.1b.

Verifying Kepler's Third Law as before is simple as shown below.

$$\Omega = \frac{d\phi}{dt} = \frac{\frac{d\phi}{d\tau}}{\frac{dt}{d\tau}} = \frac{l}{e} \left(\frac{1}{r^2} \right) \left(1 - \frac{2M}{r} \right) = \frac{1}{\sqrt{27}M} \implies \Omega^2 r^3 = M, \quad (3.43)$$

where we need to use $r_{circ} = 3M$ and the relationship between l and e for circular orbits from the constraint in Equation (3.42). Figure 3.1b also shows that apart from circular orbits, photons can either scatter or inspiral.

One can approximate the apparent radius of a Schwarzschild black hole viewed infinitely far away, by shooting photons backward from an observer. At infinity, the conserved quantities just become

$$\lim_{r \rightarrow \infty} e = \lim_{r \rightarrow \infty} \frac{dt}{d\tau} = 1, \quad \lim_{r \rightarrow \infty} l = \lim_{r \rightarrow \infty} r^2 \frac{d\phi}{d\tau} = \lim_{r \rightarrow \infty} r^2 \cdot \frac{-b}{r^2} \frac{dr}{d\tau} = b, \quad (3.44)$$

where one uses that $\dot{r} = -1$ infinitely far away (the photon just travels radially at the speed of light in asymptotically flat spacetime) and in the expression for l , one can use the small angle approximation and set $\phi = \frac{b}{r}$, where b is the impact parameter. It represents the perpendicular distance between the photon at infinity and the Schwarzschild black hole. For the photon to inspiral, one requires from Equation (3.42) that

$$\frac{e^2}{2} \geq \frac{l^2}{54M^2} \implies \frac{l}{e} \leq 3\sqrt{3}M \implies b \leq 5.196M. \quad (3.45)$$

Conversely, all photons with an impact parameter greater than this value starting at infinity directed inwards will scatter away. Thus a Schwarzschild black hole of mass M will appear to be $5.196 \frac{GM}{c^2}$ wide to an observer at infinity. It ultimately boils down to a competition between conserved energy and conserved angular momentum. This information is useful as a sanity check in ray tracing code for making shadows, and will also be implemented along with circular orbits in Chapter 4.

3.3 Kerr Spacetime

3.3.1 The Radial Equation

The Kerr line element which models the spacetime surrounding a rotating uncharged blackhole with mass M and angular momentum per unit mass a is repeated below for convenience,

$$ds^2 = - \left(1 - \frac{r_s r}{\Sigma} \right) dt^2 - \frac{2r_s r a \sin^2 \theta}{\Sigma} dt d\phi + \frac{\Sigma}{\Delta} dr^2 + \Sigma d\theta^2 + \left(r^2 + a^2 + \frac{r_s r a^2 \sin^2 \theta}{\Sigma} \right) \sin^2 \theta d\phi^2. \quad (3.46)$$

Here $r_s = 2M$ is the corresponding Schwarzschild radius and the definitions for Σ and Δ are as follows,

$$\Sigma = r^2 + a^2 \cos^2 \theta, \quad (3.47)$$

$$\Delta = r^2 + a^2 - 2Mr. \quad (3.48)$$

The equation of radial motion derived here follows the development in [16]. Defining the conserved energy and angular momentum analogously for Kerr black holes we get,

$$E := -g_{ij} (\partial_t)^i (\dot{\gamma})^j = -g_{tt} \dot{t} - g_{t\phi} \dot{\phi}, \quad (3.49)$$

$$L := g_{ij} (\partial_\phi)^i (\dot{\gamma})^j = g_{t\phi} \dot{t} + g_{\phi\phi} \dot{\phi}. \quad (3.50)$$

The above two expressions constitutes a linear system of equations for two entries of the four-velocity vector \dot{t} and $\dot{\phi}$. Uncoupling them using elementary methods yields the following,

$$\frac{dt}{d\tau} = \frac{E g_{\phi\phi} + L g_{t\phi}}{g_{t\phi}^2 - g_{tt} g_{\phi\phi}}, \quad (3.51)$$

$$\frac{d\phi}{d\tau} = -\frac{E g_{t\phi} + L g_{tt}}{g_{t\phi}^2 - g_{tt} g_{\phi\phi}}. \quad (3.52)$$

Apart from E , L and the length of the four velocity vector begin equal to $\mu = 0/ - 1$, there is a hidden symmetry associated to $\dot{\theta}$. The Carter constant Q found by Brandon Carter reads as

$$Q = \left(\Sigma \frac{d\theta}{d\tau} \right)^2 + \cos^2(\theta) \left(a^2(-\mu - E^2) + \frac{L^2}{\sin^2(\theta)} \right). \quad (3.53)$$

We will seek a radial equation of motion as before using $\dot{\gamma} \cdot \dot{\gamma} = \mu$, but omit usage of the Carter Constant in the calculation, because of the general kinds of stationary and axisymmetric spacetimes explored in Chapter 6. Nevertheless, verifying the preservation of the Carter Constant is a good consistency check for numerical ray tracing in Kerr spacetime. So beginning as before with $\mu = -1$ for massive particles and $\mu = 0$ for photons,

$$g(\dot{\gamma}, \dot{\gamma}) = \mu, \quad (3.54)$$

$$g_{tt}\dot{t}^2 + 2g_{t\phi}\dot{t}\dot{\phi} + g_{rr}\dot{r}^2 + g_{\theta\theta}\dot{\theta}^2 + g_{\phi\phi}\dot{\phi}^2 = \mu. \quad (3.55)$$

Substituting the expressions for \dot{t} and $\dot{\phi}$ from Equations (3.51) and (3.52) we get, after defining $W := g_{t\phi}^2 - g_{tt}g_{\phi\phi}$

$$g_{tt} \frac{(Eg_{\phi\phi} + Lg_{t\phi})^2}{W^2} - 2g_{t\phi} \frac{(Eg_{\phi\phi} + Lg_{t\phi}) \cdot (Eg_{t\phi} + Lg_{tt})}{W^2} + g_{rr}\dot{r}^2 + g_{\theta\theta}\dot{\theta}^2 + g_{\phi\phi} \frac{(Eg_{t\phi} + Lg_{tt})^2}{W^2} = \mu. \quad (3.56)$$

Re-arranging slightly and defining the Hamiltonian as before we get

$$H := \dot{r}^2 + \dot{\theta}^2 \frac{g_{\theta\theta}}{g_{rr}} + V_{eff}(r, \theta, E, L) = 0. \quad (3.57)$$

Working more on the effective potential gives then

$$V_{eff} = \frac{1}{g_{rr}} \left(-\mu + \frac{(g_{tt}(Eg_{\phi\phi} + Lg_{t\phi})^2 - 2g_{t\phi}(Eg_{\phi\phi} + Lg_{t\phi}) \cdot (Eg_{t\phi} + Lg_{tt}) + g_{\phi\phi}(Eg_{t\phi} + Lg_{tt})^2)}{W^2} \right), \quad (3.58)$$

and expanding the numerator and factoring yields

$$V_{eff} = \frac{1}{g_{rr}} \left(-\mu - W \cdot \left(\frac{E^2g_{\phi\phi} + L^2g_{tt} + 2ELg_{t\phi}}{W^2} \right) \right) = \frac{1}{g_{rr}} \left(-\mu + \frac{E^2g_{\phi\phi} + L^2g_{tt} + 2ELg_{t\phi}}{-W} \right). \quad (3.59)$$

Recalling the definition of W as set before finishes the derivation

$$V_{eff} = \frac{1}{g_{rr}} \left(-\mu + \frac{E^2g_{\phi\phi} + L^2g_{tt} + 2ELg_{t\phi}}{g_{tt}g_{\phi\phi} - g_{t\phi}^2} \right), \quad (3.60)$$

and the explicit formulae then for the massive and massless cases are respectively given by

$$V_{eff} = \frac{1}{g_{rr}} \left(1 + \frac{E^2g_{\phi\phi} + L^2g_{tt} + 2ELg_{t\phi}}{g_{tt}g_{\phi\phi} - g_{t\phi}^2} \right), \quad (3.61)$$

$$V_{eff} = \frac{1}{g_{rr}} \left(\frac{E^2g_{\phi\phi} + L^2g_{tt} + 2ELg_{t\phi}}{g_{tt}g_{\phi\phi} - g_{t\phi}^2} \right). \quad (3.62)$$

3.3.2 Photon Orbits

Seeking photon orbits in Kerr spacetime follows the same spirit as in Schwarzschild spacetime. Using the conserved quantities Q, E, L defined previously and that $\dot{\gamma} \cdot \dot{\gamma} = 0$, one finds a radial expression involving just \dot{r} , analogous to Equation (3.26). This calculation along with taking the derivative and setting it to zero to find the critical points is omitted here, and the end result found in [6] is that spherical photon orbits must obey the following

$$\frac{L}{E}|_{circ} = -\frac{r^3 - 3Mr^2 + a^2r + a^2M}{a(r - M)}, \quad (3.63)$$

$$\frac{Q}{E^2}|_{circ} = -\frac{r^3(r^3 - 6Mr^2 + 9M^2r - 4a^2M)}{a^2(r - M)^2}, \quad (3.64)$$

where r in the above expressions is restricted to lie within the following radii

$$r_1 = 2M \left[1 + \cos \left(\frac{2}{3} \cos^{-1} \left(-\frac{a}{M} \right) \right) \right] \leq r \leq 2M \left[1 + \cos \left(\frac{2}{3} \cos^{-1} \left(\frac{a}{M} \right) \right) \right] = r_2. \quad (3.65)$$

So after picking a Kerr black hole with angular momentum J and mass M , spherical photon geodesics are located in between r_1 and r_2 . Orbit located exactly at r_1 or r_2 are confined to the equatorial plane. Co-rotating spherical orbits (in the sense of a compared to L) are found in the range $r_1 \leq r < r_m$, with r_m defined as below, whereas counter-rotating spherical orbits are found in the remaining range $r_m < r \leq r_2$. Orbit confined to r_m have zero conserved angular momentum, $L = 0$.

$$r_m = M + 2\sqrt{M^2 - \frac{1}{3}a^2} \cos \left(\frac{1}{3} \cos^{-1} \left(\frac{M(M^2 - a^2)}{(M^2 - \frac{a^2}{3})^{\frac{3}{2}}} \right) \right). \quad (3.66)$$

A specific choice of r then sets the ratios in Equations (3.63) and (3.64). A choice of E then sets L and Q . This completely determines the initial conditions for a spherical photon trajectory. This technique will be key when ray tracing code in Kerr spacetime is checked for correctness, since analytical results are typically hard to obtain in this setting.

As was the case for Schwarzschild black holes, the photon region sets the apparent horizon of a Kerr black hole. Based on the conditions in Equations (3.63) and (3.64), and the range of spherical orbits in Equation (3.65), the rim of a Kerr black hole's shadow can be parametrized as below [35],

$$x = -\frac{\zeta}{\sin(\theta)}, \quad y = \pm \sqrt{\eta - \cos^2 \theta \left(\frac{\zeta^2}{\sin^2 \theta} - a^2 \right)}, \quad (3.67)$$

where ζ and η are the ratios $\frac{L}{E}$ and $\frac{Q}{E^2}$ as given in Equations (3.63) and (3.64), and θ is the observer's polar coordinate. Figure 3.2 compares the apparent horizons for Kerr black holes with varying spin for $\theta = \frac{\pi}{2}$. Starting from a circular Schwarzschild horizon, frame-dragging produces an apparent horizon that resembles the alphabet D.

3.3.3 Massive Particle Orbits

One of the trademark features of geodesics in Kerr spacetime is the forced angular velocity imparted to trajectories starting with zero orbital angular momentum L . To see this explicitly, we calculate for $L = 0$,

$$\Omega|_{L=0} = \frac{d\phi}{dt}|_{L=0} = \frac{\frac{d\phi}{dt}}{\frac{dr}{d\tau}}|_{L=0} = -\frac{g_{t\phi}}{g_{\phi\phi}} = \frac{2Mar}{(r^2 + a^2)^2 - a^2\Delta\sin^2\theta}, \quad (3.68)$$

signifying the frame dragging effect. The frame dragging of Kerr spacetime can be so severe that there exists a region where massive particles and photons are forced to co-rotate with the spin of the black hole. The ergoregion for massive particles is obtained by setting $g_{tt} > 0$, as the solution to this constraint represents the region where massive particles must necessarily be moving/non-stationary to preserve the condition that their four velocity be normalized, $\dot{\gamma} \cdot \dot{\gamma} = -1$. Doing so gives

$$g_{tt} = -\left(1 - \frac{r_s r}{\Sigma}\right) > 0, \quad (3.69)$$

$$r^2 + a^2\cos^2\theta - 2Mr < 0, \quad (3.70)$$

The above quadratic equation is negative for r in between its two roots, so the ergoregion is sandwiched in between the values,

$$\frac{2M - \sqrt{4M^2 - 4a^2\cos^2\theta}}{2} \leq r \leq \frac{2M + \sqrt{4M^2 - 4a^2\cos^2\theta}}{2}, \quad (3.71)$$

$$M - \sqrt{M^2 - a^2\cos^2\theta} \leq r \leq M + \sqrt{M^2 - a^2\cos^2\theta}. \quad (3.72)$$

In summary, we will numerically verify in Chapter 4 that null geodesics travelling in a spherical region do obey the constraints of Equations (3.63) and (3.64), and that massive particles are forced to co-rotate when they enter the region in Equation (3.72).

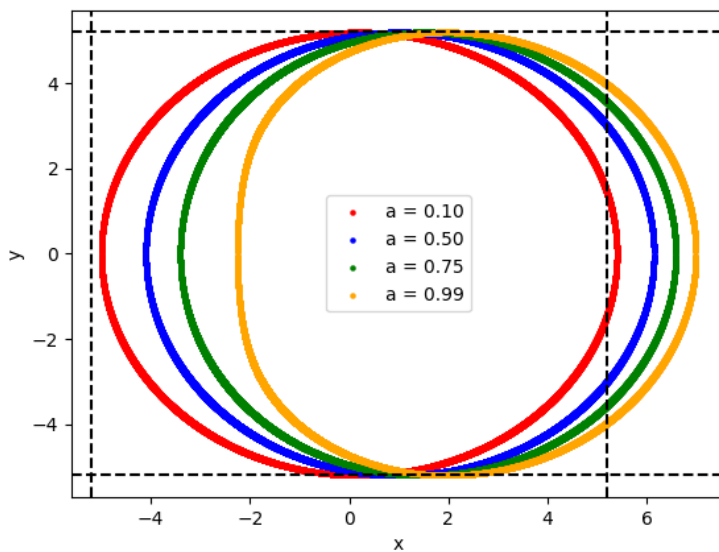


Figure 3.2: The rim of the apparent horizon for Kerr black holes with varying angular momentum. The dashed black line corresponds to the rim of a Schwarzschild black hole, found to be about $5.196M$. Due to frame-dragging, increased angular momentum produces an apparent horizon that resembles the alphabet D. The observer is located at $\theta = \frac{\pi}{2}$.

Chapter 4

Ray Tracing with Analytical Metrics

The focus now is to utilize the equations derived in Chapter 3 to visualize the trajectory of massive particles and photons in Schwarzschild and Kerr spacetimes. The equations of motion are non-linear and require numerical integration, so the chapter starts with the general methodology of the Runge Kutta style of ODE integration. The equations of motion are integrated using an adaptive Runge Kutta fourth-fifth order routine, so an analysis on its performance in terms of the error accumulated in the Hamiltonian is performed for prototypical orbits in Schwarzschild and Kerr spacetimes. After verifying theoretical expectations from Chapter 3, a recipe to make shadows of these black holes is discussed and results are presented.

4.1 Runge Kutta Integrators and Adaptive Time Stepping

Whether one uses the geodesic equation in (3.1) or the first order integrals of motion derived in Chapter 3, both routes require solving differential equations. As we will see in the recipes for ray tracing to follow, these are highly non-linear and require a numerical route for integration. The chosen style was an explicit and adaptive Runge Kutta fourth-fifth order scheme, and this section builds towards its development.

Suppose we want to solve an ODE of the form,

$$\frac{dy}{dx} = f(x, y). \quad (4.1)$$

For a step size h , Taylor expansion up to the fifth order gives the result,

$$y_{n+1} = y_n + h f(x_n, y_n) + \frac{h^2}{2} f^{(1)}(x_n, y_n) + \frac{h^3}{6} f^{(2)}(x_n, y_n) + \frac{h^4}{24} f^{(3)}(x_n, y_n) + \mathcal{O}(h)^5. \quad (4.2)$$

The Runge-Kutta integration style provides a way to by-pass the need to calculate higher-order derivatives of the function $f(x, y)$ to maintain the desired accuracy of $\mathcal{O}(h)^5$. This is done by making an ansatz of the solution, which is of the form

$$y_{n+1} = y_n + C_1 k_1 + C_2 k_2 + C_3 k_3 + C_4 k_4, \quad (4.3)$$

with C_1, C_2, C_3, C_4 constant, and the slopes k_1, k_2, k_3, k_4 are given by

$$k_1 = h f(x_n, y_n), \quad (4.4)$$

$$k_2 = h f(x_n + A_2 h, y_n + B_{21} k_1), \quad (4.5)$$

$$k_3 = h f(x_n + A_3 h, y_n + B_{31} k_1 + B_{32} k_2), \quad (4.6)$$

$$k_4 = h f(x_n + A_4 h, y_n + B_{41} k_1 + B_{42} k_2 + B_{43} k_3). \quad (4.7)$$

Comparing the ansatz with the Taylor expansion paves the way to solve for the 13 unknown constants. The system of equations is over-determined, and the right choice of constants can produce a symmetric result. The most popularly-used form of the RK-4 integrator is the following

$$y_{n+1} = y_n + \frac{1}{6} \left(h f(x_n, y_n) + 2 h f\left(x_n + \frac{h}{2}, y_n + \frac{k_1}{2}\right) + 2 h f\left(x_n + \frac{h}{2}, y_n + \frac{k_2}{2}\right) + h f(x_n + h, y_n + k_3) \right). \quad (4.8)$$

The intuition behind Equation (4.8) is as follows. First one calculates the slope with the initial point, uses it to find two slopes at the half way points, and then jumps to the final value with the third slope. The half-way slopes are doubly weighted compared to the boundary slopes in the final calculation of the next value of the dependent variable y . The local truncation error is proportional to $\mathcal{O}(h)^5$, and this translates to a global accumulated error proportional to $N \times \mathcal{O}(h)^5 \propto \mathcal{O}(h)^4$, since $N = \frac{\text{end} - \text{start}}{h} + 1$. In the context of geodesic integration, a numerical integrator will get away with a larger step size h far away from the event horizon, where the metric and its derivatives don't change rapidly, but will require a smaller step size closer to the event horizon where typically the component g_{rr} starts to become singular. Thus it is desirable to have a routine that dynamically changes the step size depending on where the particle is in its trajectory. General adaptive time stepping is done by calculating the error of the current step and setting the step size accordingly for the next step if the error is within tolerance, or re-doing the current step with the re-calculated step size. Using pure fourth-order Runge Kutta integration, this is typically implemented by first calculating the new value of the dependent variable y_{n+1} with a step size h , and then halving the step size and finding the value y_{n+1}^* after two rounds of integration [36]. Approximating y_{n+1}^* as the true solution, the error $\epsilon_1 = |y_{n+1} - y_{n+1}^*|$ is calculated. If the desired tolerance is ϵ_2 , and $\epsilon_1 > \epsilon_2$, the step is performed again with step size h_2 equal to

$$h_2 = h_1 \left(\frac{\epsilon_2}{\epsilon_1} \right)^{\frac{1}{5}}, \quad (4.9)$$

where the simple fact that $\epsilon \propto h^5$ is used. If $\epsilon_1 < \epsilon_2$, Equation (4.9) sets the step size for the next iteration step. An alternate and common way to set the step size is to halve it when $\epsilon_1 > \epsilon_2$, or double it if $\epsilon_1 < \epsilon_2$. In either scenario, a minimum and maximum value for the possible values of h should be chosen, because a very small step size would slow down the particle's motion and increase integration time to an unfeasible amount, whereas a very big step size might even render the true solution y_{n+1}^* inaccurate.

The adaptive time stepping discussed so far relies on three rounds of fourth order Runge Kutta integration, one to find y_{n+1} and two to find y_{n+1}^* , which can be resource-consuming for large periods of integration. The embedded Runge-Kutta-Cash-Karp Method provides a more efficient way to approximate the true solution with fewer number of evaluations [36]. The Butcher Table for the fourth-fifth order scheme is given in Table 4.1. The convention for the ordinary 4th order Runge Kutta integra-

i	A_i	B_{i1}	B_{i2}	B_{i3}	B_{i4}	B_{i5}	C_i	C_i^*
1							$\frac{37}{378}$	$\frac{2825}{27648}$
2	$\frac{1}{5}$	$\frac{1}{5}$					0	0
3	$\frac{3}{10}$	$\frac{3}{40}$	$\frac{9}{40}$				$\frac{250}{621}$	$\frac{18575}{48384}$
4	$\frac{3}{5}$	$\frac{3}{10}$	$-\frac{9}{10}$	$\frac{6}{5}$			$\frac{125}{594}$	$\frac{13525}{55296}$
5	1	$-\frac{11}{54}$	$\frac{5}{2}$	$-\frac{70}{27}$	$\frac{35}{27}$		0	$\frac{277}{14336}$
6	$\frac{7}{8}$	$\frac{1631}{55296}$	$\frac{175}{512}$	$\frac{575}{13824}$	$\frac{44275}{110592}$	$\frac{253}{4096}$	$\frac{512}{1771}$	$\frac{1}{4}$

Table 4.1: Cash-Karp Table for Embedded RK 4-5 Scheme

tion is maintained in 4.1, where the coefficients C_i^* now correspond to the fourth order scheme and C_i corresponds to the fifth order scheme which also approximates the true solution. We can see that the slope-related constants A_i and B_{ij} for each order scheme are the same, and they only differ in the weighting constants C_i and C_i^* , thereby greatly reducing the number of calculations required to develop a notion of error at each iteration, which is just the difference in the six evaluations

$$err_1 = \sum_{i=1}^6 k_i (C_i - C_i^*), \quad (4.10)$$

and is the error of the fourth order scheme. In our scenario of interest, we have multiple variables, say m many that each have an error err_{1m} . Suppose then we desire a maximum error in each variable, equal to err_{2m} . A good method to average the total error for coupled ordinary differential equations is to use the Euclidean norm [36], and define the net error as follows,

$$\epsilon_1 = \sqrt{\frac{1}{m} \sum_m \left(\frac{err_{1m}}{err_{2m}} \right)^2}. \quad (4.11)$$

$\epsilon_1 \leq 1$ is then taken as an acceptable iteration step. So finally, Equation (4.9) can then be used to find the ideal step size h_2 assuming a desired tolerance of $\epsilon_2 = 1$. Explicitly, the ideal step size is then

$$h_2 = h_1 \left(\frac{1}{\epsilon_1} \right)^{\frac{1}{5}}. \quad (4.12)$$

In practice, adaptive step sizing using embedded methods Runge-Kutta methods could suffer from the approximation of the true solution becoming inaccurate itself. In the context of ray tracing, this can happen when the particle spends too much time close to the compact object. It then becomes difficult to develop any notion of a true solution and adjust the step size with respect to it. Thus in this work, the spacetime is split into four sections, $r \leq 3M$, $3M < r \leq 10M$, $10M < r \leq 50M$ and $50M < r$ that correspond to step sizes 10^{-3} , 10^{-2} , 5×10^{-2} and 10^{-1} respectively. Then to achieve maximum accuracy, the fifth order solution from the Runge-Kutta Cash-Karp Table is used directly.

4.2 Recipe and Results in Schwarzschild Spacetime

Fixing the plane of the orbit to be $\theta = \frac{\pi}{2}$, the reduced list of kinematic variables is $t, \phi, r, \dot{t}, \dot{\phi}, \dot{r}$. Equations (3.18) and (3.19) provide an elegant way to introduce conserved quantities in the set up and solve for t, ϕ , where as Equation (3.25) is the relevant equation for radial motion. The issue is that it is an expression for \dot{r}^2 , so there is an ambiguity with which sign of the square root to select. Additionally, square roots always suffer from the problem of encountering negative entries in numerical schemes, so this approach should be avoided. An easy way to remove the square root is to just take an additional derivative, and doing so one arrives at,

$$0 = \dot{r}\ddot{r} - \frac{l^2}{r^3}\dot{r} - \frac{M\mu}{r^2}\dot{r} + \frac{3Ml^2}{r^4}\dot{r} \implies \ddot{r} = \frac{l^2}{r^3} + \frac{M\mu}{r^2} - \frac{3Ml^2}{r^4}. \quad (4.13)$$

The price paid is that we now have to solve a second order differential equation for r . This is done by decomposing it into two first order differential equations. Thus, the complete recipe and relevant equations to numerically create trajectories in Schwarzschild spacetime is as follows:

- Pick a value of l and M , and plot the effective potentials for massive particles or photons, given again below as

$$V_{eff} = \frac{l^2}{2r^2} + \frac{M\mu}{r} - \frac{Ml^2}{r^3}, \quad \mu = 0/ - 1. \quad (4.14)$$

- Know which kinds of orbits are possible for the chosen value of l . Interesting orbits for massive particles occur at $l > \sqrt{12}M$, whereas photons have a fixed shape of their potential. Choose which kind of orbit is desired, by picking the value of the Hamiltonian, repeated below,

$$\frac{e^2 + \mu}{2} = \frac{1}{2}\dot{r}^2 + \frac{l^2}{2r^2} + \frac{M\mu}{r} - \frac{Ml^2}{r^3}, \quad \mu = 0/ - 1, \quad (4.15)$$

and doing this sets the value of e .

- Set initial conditions. There is complete freedom in specifying the initial t_0, ϕ_0 , but the value of r_0 is picked from the allowed region, read from the potential diagram. The initial velocities are then found using,

$$t_0 = \frac{e}{\left(1 - \frac{2M}{r_0}\right)}, \quad \dot{\phi}_0 = \frac{l}{r_0^2}, \quad \dot{r}_0 = \pm \sqrt{2 \left(\frac{e^2 + \mu}{2} - V_{eff} \right)}. \quad (4.16)$$

There is freedom in choosing the sign of \dot{r}_0 , specifying an ingoing or outgoing trajectory. For circular orbits, it is best practice to set $\dot{r}_0 = 0$ manually.

- Solve the following system of equations using a numerical integrator.

$$\frac{dt}{d\tau} = \frac{e}{\left(1 - \frac{2M}{r}\right)}, \quad (4.17)$$

$$\frac{d\phi}{d\tau} = \frac{l}{r^2}, \quad (4.18)$$

$$\frac{dv_r}{d\tau} = \frac{l^2}{r^3} + \frac{M\mu}{r} - \frac{3Ml^2}{r^4}, \quad \frac{dr}{d\tau} = v_r. \quad (4.19)$$

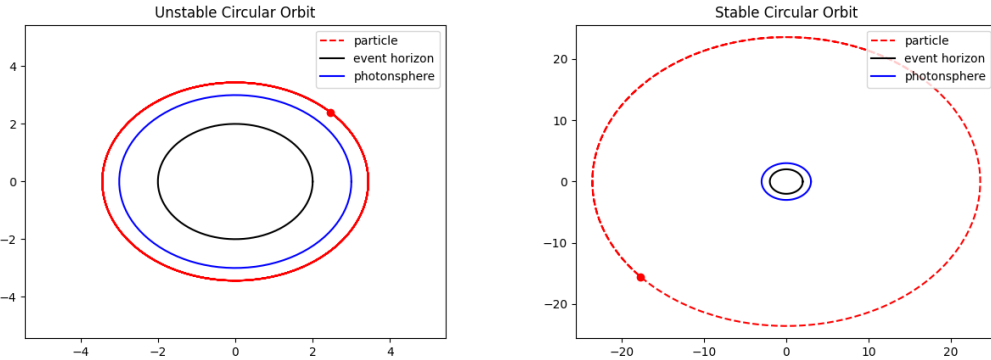
- To check accuracy, store the result of the following quantity below at every time step i . This is the deviation from expected zero at every iteration.

$$H_i = \left| \frac{e^2 + \mu}{2} - \frac{1}{2} \dot{r}_i^2 - V_{eff,i} \right|, \quad \bar{H} = \frac{1}{N} \sum_i^N H_i, \quad (4.20)$$

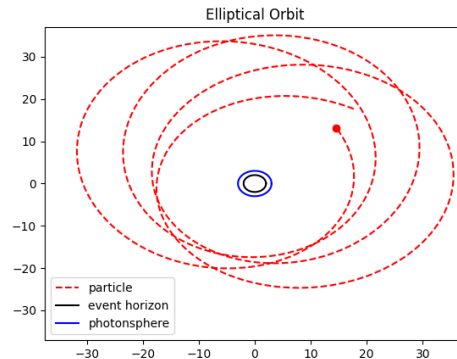
and averaging this quantity yields the net deviation from expected zero, \bar{H} . A good implementation for analytical ray tracing keeps the net deviation close to machine epsilon.

The above was implemented for the $M = 1, l = 1.5l_{crit}$ case for massive particles, with the goal of tracing the stable and unstable circular orbits and an elliptical orbit. The relevant potential diagrams are in Figure 3.1, with the dashed lines showcasing the Hamiltonian value of each desired orbit. The purple line corresponds to the unstable circular orbit, the orange line corresponds to the stable circular orbit, and the red line corresponds to an elliptical orbit. Figure 4.1 displays the trajectories generated by the numerical recipe discussed. The particle in Figure 4.1a was integrated up to $\tau = 100$, where as Figures 4.1b and 4.1c were integrated up to $\tau = 1000$ and $\tau = 3000$ respectively. It was observed that all orbits maintained their desired properties. The corresponding orders of magnitude of \bar{H} were equal to 10^{-15} , 10^{-18} and 10^{-17} for the unstable circular, stable circular and elliptical trajectories respectively.

The photon sphere orbit corresponding to $M = 1, l = 1$ was traced along with two photons above and below it in the effective potential diagram, all shown in Figure 3.1b. The expectation is for the photon with the energy of the purple line to inspiral, the one with energy given by the orange line to scatter, and for the photon marked with red that has the energy corresponding to the unstable circular orbit to wind a few times before being scattered inwards or outwards. Figure 4.2 displays the trajectories generated by the numerical recipe discussed. The trajectory in Figure 4.2a was integrated till $\tau = 100$ where as the photons shot backwards in 4.2b into the blackhole were integrated up to a final proper time of $\tau = 1000$. The \bar{H} for the photonsphere orbit was of the order 10^{-18} . All the trajectories in Figure 4.2b had net deviation $\bar{H} = 10^{-17}$. As expected, photons with an impact parameter greater than $\sqrt{27}M = 5.196M$ scatter, where as those with impact parameter less than this value inspiral.

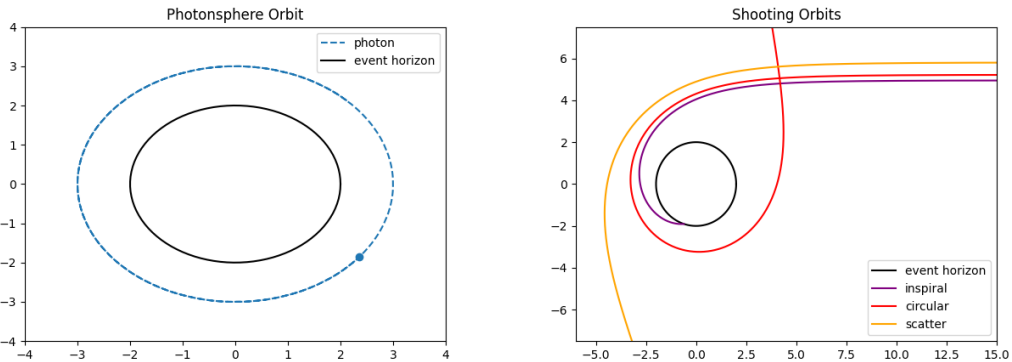


(a) Unstable Circular Orbit in Schwarzschild Spacetime (b) Stable Circular Orbit in Schwarzschild Space-time



(c) Elliptical Orbit in Schwarzschild Spacetime

Figure 4.1: The trademark trajectories of massive particles in Schwarzschild spacetime for $M = 1$ and $l = 1.5\sqrt{12}$. The unstable circular orbit was integrated till $\tau = 100$, where as the stable circular and elliptical orbits were integrated up to a final proper time of $\tau = 1000$ and $\tau = 3000$ respectively.



(a) Photon Sphere Orbit in Schwarzschild Space-time (b) Shooting Photons Backward in Schwarzschild Spacetime

Figure 4.2: Test trajectories in Schwarzschild space time for $M = 1$ and $l = 1$. On the left is the photon sphere orbit, and unstable circular orbit that is not disrupted after integrating till $\tau = 100$. On the right are photons shot inwards after adjusting their impact parameters by the ratio $\frac{l}{e}$. It is verifiable that photons with an impact parameter greater than $\sqrt{27}M = 5.196M$ scatter, where as those with impact parameter less than this value inspiral.

4.3 Recipe and Results in Kerr Spacetime

In the case of Kerr, the plane of the orbit can't simply be fixed to be $\theta = \frac{\pi}{2}$, so the full set of kinematic variables is $t, r, \theta, \phi, \dot{t}, \dot{r}, \dot{\theta}, \dot{\phi}$. The conserved quantities defined by Equations(3.49) and (3.50) solve for the motion in t and ϕ directions, and Equation(3.57) is the relevant expression for radial and polar angle motion. This time the issue of the square root can't be resolved by simply taking a derivative due to the presence of both r and θ . Also, since the aim in Chapter 5 will be to extend this Kerr treatment to general stationary and axisymmetric space times, the Carter Constant will also remain unused. Hence the geodesic equations are used to isolate for the variables \ddot{r} and $\ddot{\theta}$. To use Equation (3.1), the non-vanishing Christoffel Symbols must be calculated. For a general diagonal metric with off-diagonal entries in $dtd\phi$ having only $r - \theta$ dependence, the geodesic equations for r and θ reduce to the following as stated in [16],

$$2g_{rr}\ddot{r} + 2\dot{r}\dot{\theta}\partial_\theta g_{rr} + \dot{r}^2\partial_r g_{rr} - \dot{t}^2\partial_r g_{tt} - 2\dot{t}\dot{\phi}\partial_r g_{t\phi} - \dot{\theta}^2\partial_r g_{\theta\theta} - \dot{\phi}^2\partial_r g_{\phi\phi} = 0, \quad (4.21)$$

$$2g_{\theta\theta}\ddot{\theta} + 2\dot{r}\dot{\theta}\partial_r g_{\theta\theta} - \dot{r}^2\partial_\theta g_{rr} - \dot{t}^2\partial_\theta g_{tt} - 2\dot{t}\dot{\phi}\partial_\theta g_{t\phi} + \dot{\theta}^2\partial_\theta g_{\theta\theta} - \dot{\phi}^2\partial_\theta g_{\phi\phi} = 0. \quad (4.22)$$

The required metric coefficient derivatives are presented below in succinct form, using the definitions of (Σ, Δ) given in equations (2.10) and (2.11).

$$\partial_\theta g_{rr} = -\frac{a^2 \sin 2\theta}{\Delta}, \quad (4.23)$$

$$\partial_r g_{rr} = \frac{2(r\Delta - (r - M)\Sigma)}{\Delta^2}, \quad (4.24)$$

$$\partial_r g_{tt} = \frac{2M(\Sigma - 2r^2)}{\Sigma^2}, \quad (4.25)$$

$$\partial_r g_{t\phi} = \frac{2Ma \sin^2 \theta (2r^2 - \Sigma)}{\Sigma^2}, \quad (4.26)$$

$$\partial_r g_{\theta\theta} = 2r, \quad (4.27)$$

$$\partial_r g_{\phi\phi} = \sin^2 \theta \left(2r + \frac{2Ma^2 \sin^2 \theta (\Sigma - 2r^2)}{\Sigma^2} \right), \quad (4.28)$$

$$\partial_\theta g_{tt} = \frac{2Mra^2 \sin 2\theta}{\Sigma^2}, \quad (4.29)$$

$$\partial_\theta g_{t\phi} = -\frac{2Mr a \sin 2\theta (\Sigma + a^2 \sin^2 \theta)}{\Sigma^2}, \quad (4.30)$$

$$\partial_\theta g_{\theta\theta} = -a^2 \sin 2\theta, \quad (4.31)$$

$$\partial_\theta g_{\phi\phi} = g_{\phi\phi} \frac{\sin 2\theta}{\sin^2 \theta} + \frac{2mra^2 \sin^2 \theta \sin 2\theta (\Sigma + a^2 \sin^2 \theta)}{\Sigma^2}. \quad (4.32)$$

Below is a recipe to trace trajectories of massive particles and photons in Kerr spacetime, with relevant equations repeated for easy reference.

- Pick a value of a, M, E, L , and plot the effective potential for massive particles or photons, given again below as,

$$V_{eff} = \frac{1}{g_{rr}} \left(-\mu + \frac{E^2 g_{\phi\phi} + L^2 g_{tt} + 2EL g_{t\phi}}{g_{tt} g_{\phi\phi} - g_{t\phi}^2} \right), \quad \mu = 0 / -1. \quad (4.33)$$

- Ascertain which is the allowed region by isolating areas in the $r - \theta$ plane where $V_{eff} < 0$, as this implies that $\dot{r}^2 + \frac{g_{\theta\theta}}{g_{rr}}\dot{\theta}^2 > 0$ here as a consequence of Equation (3.57).
- Set initial conditions. There is again complete freedom in choosing t_0, ϕ_0 where as r_0, θ_0 are picked from the allowed region. The initial velocities are then given by,

$$\dot{t}_0 = \frac{E g_{\phi\phi} + L g_{t\phi}}{g_{t\phi}^2 - g_{tt} g_{\phi\phi}}, \quad \dot{\phi}_0 = -\frac{E g_{t\phi} + L g_{tt}}{g_{t\phi}^2 - g_{tt} g_{\phi\phi}}, \quad \dot{r}_0^2 + \dot{\theta}_0^2 \frac{g_{\theta\theta}}{g_{rr}} + V_{eff}(r_0, \theta_0, E, L) = 0. \quad (4.34)$$

The degeneracy in picking $\dot{r}_0, \dot{\theta}_0$ is broken by a choice of the Carter Constant given by

$$Q = \left(\Sigma \dot{\theta}_0 \right)^2 + \cos^2(\theta_0) \left(a^2(-\mu - E^2) + \frac{L^2}{\sin^2(\theta_0)} \right). \quad (4.35)$$

Calculating the Carter Constant at the beginning of numerical integration allows checking that it is indeed a conserved quantity.

- Solve the following equations of motion using a numerical integrator.

$$\frac{dt}{d\tau} = \frac{Eg_{\phi\phi} + Lg_{t\phi}}{g_{t\phi}^2 - g_{tt}g_{\phi\phi}}, \quad (4.36)$$

$$\frac{d\phi}{d\tau} = -\frac{Eg_{t\phi} + Lg_{tt}}{g_{t\phi}^2 - g_{tt}g_{\phi\phi}}, \quad (4.37)$$

$$\frac{dv_r}{d\tau} = \frac{-1}{2g_{rr}} \left(2\dot{r}\dot{\theta}\partial_\theta g_{rr} + \dot{r}^2\partial_r g_{rr} - \dot{t}^2\partial_r g_{tt} - 2\dot{t}\dot{\phi}\partial_r g_{t\phi} - \dot{\theta}^2\partial_r g_{\theta\theta} - \dot{\phi}^2\partial_r g_{\phi\phi} \right), \quad \frac{dr}{d\tau} = v_r, \quad (4.38)$$

$$\frac{dv_\theta}{d\tau} = \frac{-1}{2g_{\theta\theta}} \left(2\dot{r}\dot{\theta}\partial_r g_{\theta\theta} - \dot{r}^2\partial_\theta g_{rr} - \dot{t}^2\partial_\theta g_{tt} - 2\dot{t}\dot{\phi}\partial_\theta g_{t\phi} + \dot{\theta}^2\partial_\theta g_{\theta\theta} - \dot{\phi}^2\partial_\theta g_{\phi\phi} \right), \quad \frac{d\theta}{d\tau} = v_\theta, \quad (4.39)$$

where the derivatives of the metric have been calculated previously.

- To check accuracy, store the result of the following quantity below every time step i . This is the deviation from expected zero at every iteration.

$$H_i = \left| \dot{r}^2 + \dot{\theta}^2 \frac{g_{\theta\theta}}{g_{rr}} + V_{eff,i} \right|, \quad \bar{H} = \frac{1}{N} \sum_i^N H_i \quad (4.40)$$

Averaging this quantity yields the net deviation of the Hamiltonian from expected zero, \bar{H} . A good implementation for analytical ray tracing keeps the net deviation close to machine epsilon.

Fixing $M = 1, a = 0.5$, three spherical photon orbits were traced using the above recipe. Using Equation (3.65) it was found that spherical photon orbits exist between $2.34 \leq r \leq 3.53$. Radii of $r = 2.5, 2.7, 3.0$ were picked for simulation, and the corresponding constraints on E, L, Q were found using Equations (3.63) and (3.64). Figures 4.3a, 4.3b and 4.3c display the simulated trajectory up till a final proper time of $\tau = 100$. The value of \bar{H} in these three cases was of the order $10^{-15}, 10^{-14}$ and 10^{-13} respectively, and the deviation in the average numeric value of the Carter Constant compared to the initially found value was equal to $10^{-13}, 10^{-13}$ and 10^{-12} respectively. In all three cases, E was set to be $\frac{1}{3}$, thereby determining the value of L via Equation 3.63. Setting the value of $\dot{r}_0 = 0$ determined $\dot{\theta}_0$ using Equation (3.62) which sets the Carter Constant via Equation (3.53). This value of Q equals the value obtained from Equation 3.64, with $E = \frac{1}{3}$. The right panel for each of these plots shows the effective potential defined by Equation (3.62), and the allowed regions are shaded in dark blue and green. It confirms that spherical photon orbits in Kerr spacetime are unstable, because a slight perturbation could send the photon to infinity or cause it to inspiral.

Massive particles in the spacetime of a Kerr black hole with $M = 1, a = 0.5$ were also simulated, to see the effect of the ergoregion discussed in Chapter 3. Three orbits with $L = 0, -1, -2$ were traced and the trajectories are shown in Figure (4.3d). For all three cases, \bar{H} and the deviation of the Carter Constant was on the order of 10^{-10} . It is verifiable that they all change their direction of rotation when they reach within the ergoregion.

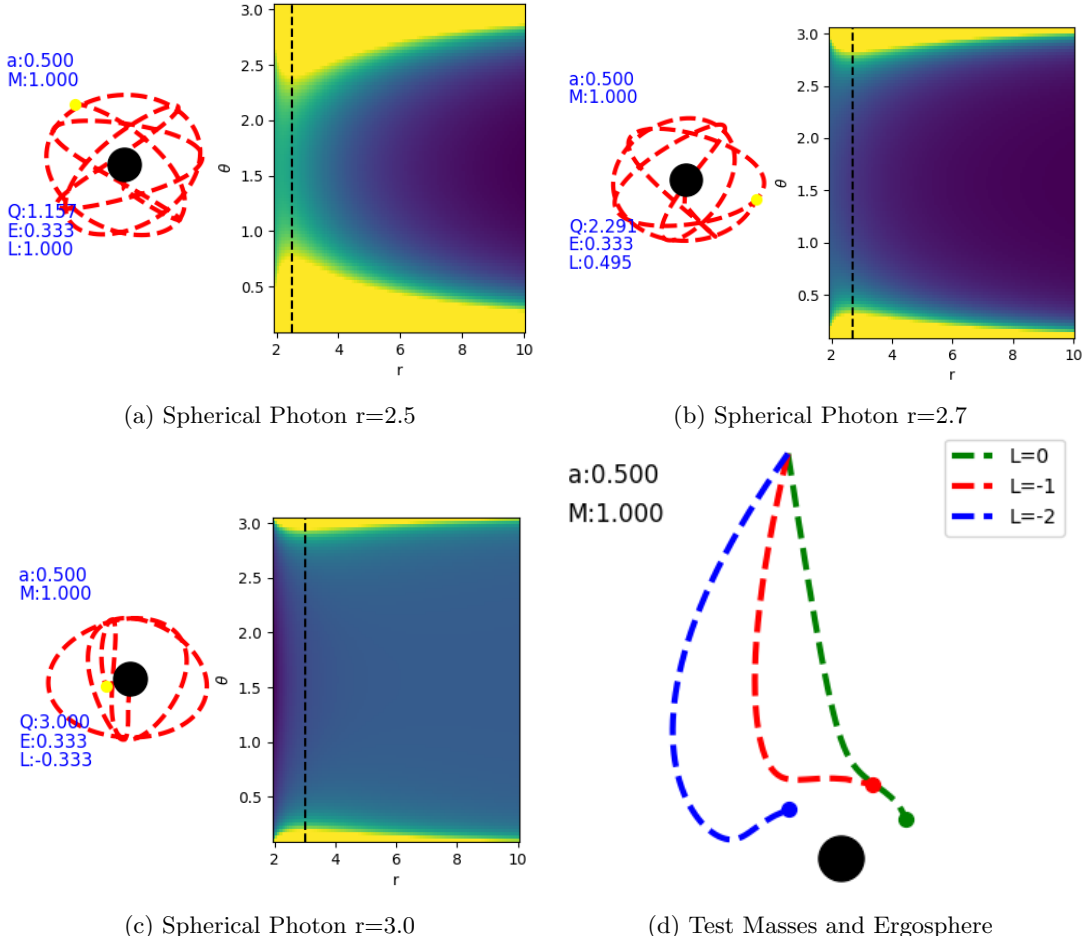


Figure 4.3: Three spherical photon orbits and turning of massive test particles in a Kerr spacetime with $M = 1$ and $a = 0.5$. The initial conditions for 4.3a, 4.3b and 4.3c are labelled on the plots; each ray was integrated till a proper time of $\tau = 100$. The net deviation from expected zero in \bar{H} was of the order 10^{-15} , 10^{-14} and 10^{-13} respectively, where as the deviation of Q from original was of the order 10^{-13} , 10^{-13} and 10^{-12} respectively. The right panels shows V_{eff} in the $r - \theta$ plane with the allowed region shaded in dark blue-green. The dashed line shows the radial location of the orbit traced. The photon is free to move in a very large domain of r , thereby signifying the unstable character of this orbit. 4.3d shows the behaviour of massive particles before and after entering the ergoregion. The three test masses were given a value of L opposite or neutral compared to the sign of the black hole's angular momentum. Journeying inwards, the test masses begin to co-rotate with the black hole because of the intense rotational influence of the Kerr black hole's spin.

4.4 Shadows of Schwarzschild and Kerr Black Holes

4.4.1 Local Orthonormal Basis and Recipe

To construct the gravitationally lensed background of a black hole, ray tracing for many photons originating at the observer was implemented, integrating the equations of motion backward in time. This methodology of backward ray tracing is more advantageous than shooting photons from the background, since the latter technique may waste considerable time evolving photons that don't make it to the observer's screen. The formalism developed here follows the techniques discussed in [35], in which Lora et al. discuss their code OSIRIS used for ray tracing around compact objects.

Armed with a numerical recipe to integrate the equations of motion, the only missing ingredient is finding the right initial conditions. This is done by introducing two angles α and β which denote the impact parameter of a starting photon, and calculating values in a local orthonormal basis. Figure 4.4 pictorially shows the set up. With the convention of the angles α and β adopted in this Figure, the impact parameters are given by,

$$x = -r_0 \sin \beta, \quad y = r_0 \sin \alpha. \quad (4.41)$$

Then, the components of the spatial momentum in the observer's frame of reference in terms of these angles are given by,

$$\mathcal{P}^r = |\vec{\mathcal{P}}| \cos \alpha \cos \beta, \quad \mathcal{P}^\theta = |\vec{\mathcal{P}}| \sin \alpha, \quad \mathcal{P}^\phi = |\vec{\mathcal{P}}| \cos \alpha \sin \beta, \quad (4.42)$$

and the photon has $\mathcal{P}^t = |\vec{\mathcal{P}}|$. Since $|\vec{\mathcal{P}}|$ does not impact geodesic tracing, it is set to unity, meaning that $\mathcal{P}^t = 1$ as well.

We must now connect the components of the 4-momentum in the general curved coordinates (which in the current scenario are the Schwarzschild and Kerr coordinates), to the quantities $\mathcal{P}^t, \mathcal{P}^r, \mathcal{P}^\theta, \mathcal{P}^\phi$. This requires knowledge of how the basis vectors look like in the local orthonormal basis. The basis picked is of the following form,

$$\hat{e}_\theta = A^\theta \partial_\theta, \quad \hat{e}_\phi = A^\phi \partial_\phi, \quad \hat{e}_t = \zeta \partial_t + \gamma \partial_\phi, \quad \hat{e}_r = A^r \partial_r. \quad (4.43)$$

Now imposing that $\hat{e}_r \cdot \hat{e}_r = 1, \hat{e}_\theta \cdot \hat{e}_\theta = 1, \hat{e}_\phi \cdot \hat{e}_\phi = 1$, we simply arrive at

$$A^r = \frac{1}{\sqrt{g_{rr}}}, \quad A^\theta = \frac{1}{\sqrt{g_{\theta\theta}}}, \quad A^\phi = \frac{1}{\sqrt{g_{\phi\phi}}}. \quad (4.44)$$

Lastly, ζ and γ can be determined using the conditions $\hat{e}_t \cdot \hat{e}_t = -1$ and $\hat{e}_t \cdot \hat{e}_\phi = 0$. Using the latter condition we get that,

$$0 = \hat{e}_t \cdot \hat{e}_\phi = \zeta A^\phi g_{t\phi} + \gamma A^\phi g_{\phi\phi}, \quad (4.45)$$

$$0 = \zeta \frac{g_{t\phi}}{\sqrt{g_{\phi\phi}}} + \gamma \sqrt{g_{\phi\phi}} \implies \gamma = -\zeta \frac{g_{t\phi}}{g_{\phi\phi}}, \quad (4.46)$$

and substituting into the former condition gives that,

$$-1 = \hat{e}_t \cdot \hat{e}_t = \zeta^2 g_{tt} + \gamma^2 g_{\phi\phi} + 2g_{t\phi}\zeta\gamma, \quad (4.47)$$

$$-1 = \zeta^2 g_{tt} + \zeta^2 \frac{g_{t\phi}^2}{g_{\phi\phi}} - \zeta^2 2 \frac{g_{t\phi}^2}{g_{\phi\phi}}, \quad (4.48)$$

$$-1 = \zeta^2 \left(\frac{g_{tt}g_{\phi\phi} - g_{t\phi}^2}{g_{\phi\phi}} \right), \quad (4.49)$$

$$\zeta = \sqrt{\frac{g_{\phi\phi}}{g_{t\phi}^2 - g_{tt}g_{\phi\phi}}}. \quad (4.50)$$

So the final form of the four basis vectors that describe a Minkowski frame is the following,

$$\hat{e}_t = \zeta \left(\partial_t - \frac{g_{t\phi}}{g_{\phi\phi}} \partial_\phi \right), \quad \hat{e}_r = \frac{1}{\sqrt{g_{rr}}} \partial_r, \quad \hat{e}_\theta = \frac{1}{\sqrt{g_{\theta\theta}}} \partial_\theta, \quad \hat{e}_\phi = \frac{1}{\sqrt{g_{\phi\phi}}} \partial_\phi. \quad (4.51)$$

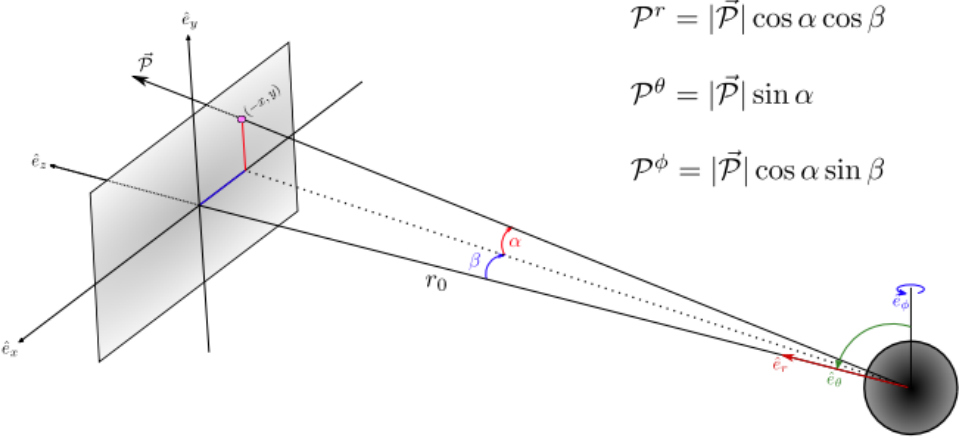


Figure 4.4: Set up of the local orthonormal frame used for backward ray tracing and shadow production as found in [35], which is also used in this work. Using two angles α and β , the components of the spatial momentum in the observer's frame are decomposed and the impact parameters are given as $x = -r_0 \sin \beta$ and $y = r_0 \sin \alpha$. This procedure sets the initial conditions of every photon intercepting the observer's screen as outlined in the script.

Using this information, we project the components of the 4-momentum into this basis as follows,

$$\mathcal{P}^t = -\hat{e}_t^\mu p_\mu = -(\zeta p_t + \gamma p_\phi) = \zeta \left(E + \frac{g_{t\phi}}{g_{\phi\phi}} L \right), \quad (4.52)$$

$$\mathcal{P}^r = \hat{e}_r^\mu p_\mu = \frac{1}{\sqrt{g_{rr}}} p_r, \quad (4.53)$$

$$\mathcal{P}^\theta = \hat{e}_\theta^\mu p_\mu = \frac{1}{\sqrt{g_{\theta\theta}}} p_\theta, \quad (4.54)$$

$$\mathcal{P}^\phi = \hat{e}_\phi^\mu p_\mu = \frac{1}{\sqrt{g_{\phi\phi}}} L, \quad (4.55)$$

where the identification of the conserved quantities $E = -p_t$, $L = p_\phi$ was used wherever they appear. Given the manner in which the numerical recipe has been developed, it is more desirable to obtain starting conditions for E, L, p^r, p^θ . Explicitly, inverting the above expressions yields,

$$E = \sqrt{\frac{g_{t\phi}^2 - g_{tt}g_{\phi\phi}}{g_{\phi\phi}}} - \mathcal{P}^\phi \frac{g_{t\phi}}{\sqrt{g_{\phi\phi}}}, \quad L = \mathcal{P}^\phi \sqrt{g_{\phi\phi}}, \quad p^r = \frac{\mathcal{P}^r}{\sqrt{g_{rr}}}, \quad p^\theta = \frac{\mathcal{P}^\theta}{\sqrt{g_{\theta\theta}}}. \quad (4.56)$$

So after picking the observer's distance to the black hole given by r_0 , the two parametrization angles α and β determine the impact parameters x, y and the starting velocities via the local orthonormal basis. For all the shadows created, the observer is placed at $\theta_0 = \frac{\pi}{2}$ and $\phi_0 = 0$. With these starting conditions, photons spread equidistant in α, β are evolved backward in time for a fixed negative final proper time. If it inspirals into the black hole, the pixel from which it originated is assigned the black colouration, where as if it does not inspiral, it encodes the information about the part of the celestial sphere it intercepts. For this purpose, the celestial sphere is divided into four equal quadrants in the following way: red for $0 < \theta < \frac{\pi}{2} \cap \pi < \phi < 2\pi$, green for $0 < \theta < \frac{\pi}{2} \cap 0 < \phi < \pi$, yellow for $\frac{\pi}{2} < \theta < \pi \cap \pi < \phi < 2\pi$ and blue for $\frac{\pi}{2} < \theta < \pi \cap 0 < \phi < \pi$.

4.4.2 Discussion of Results

Shadows of Schwarzschild and Kerr black holes were produced using local orthonormal basis construction and the colour-coding logic mentioned before. Figure 4.5 displays the results for an observer located at $(r = 15M, \theta = \frac{\pi}{2}, \phi = 0)$ for different values of the angular momentum parameter. 4.5a serves as the standard for comparison, as it is the Minkowski flat spacetime where light rays are not bent during

propagation, so the observer sees exactly the same unchanged background.

4.5c is the shadow of a Schwarzschild blackhole with $M = 1$, and we can immediately see that the apparent horizon is $r \approx 5.196M$, as was illustrated in Chapter 3. Proceeding outwards, the background appears lensed as a concentric circle around the hole; farther away from hole the background appears flat and not lensed as one would expect, as these photons don't experience strong deflections due to a larger impact parameter. 4.5b and 4.5d are the shadows of Kerr blackholes with $M = 1$ and $a = 0.5M/0.99M$ respectively. In contrast to the Schwarzschild shadow, the non-lensed part of the background now appears as though it leaks to the left. This is a consequence of frame dragging, and is reflected even in the image of the dark hole and the circular lensed region. The circular lensed region now seems to have an ear comprising of the yellow and red colours. Expectedly, the Kerr black hole with $a = 0.99$ showcases heavier frame-dragging, as it appears to have a dark hole that resembles the alphabet 'D', and has a yellow-red ear which leaks over more than the $a = 0.5$ case to the left side of the dark hole, and is bordered by a heavily lensed region. All images in Figure 4.5 were made using total backward integration till the photon hit the celestial sphere, located at $r = 15M$. A screen with 250×250 pixels was used in this thesis work, but is advisable to use a denser screen if the nature of the Einstein rings to higher resolution are desired, especially near the apparent horizon.

Apart from confirming the shape and size of the shadow to be the same as supplied by theoretical predictions, the numerical accuracy of these shadows was also tested. Figure 4.6 shows in the log scale, the deviation of the Hamiltonian and the Carter Constant. It was observed that for each case, the average Hamiltonian performs better than the Carter Constant, as it is closer to machine precision. As expected, a brighter region near the shadow appears, signalling that photons which venture close to the horizon pick up larger error in their ray tracing. Interestingly, there exists a bright vertical streak at the centre of the screen. To understand this, consult Equations 4.42 and 4.56. Photons at the central vertical strip of the screen have a vanishing angular momentum L and a high radial component of the momentum p^r owing to $\beta = 0$. Hence these photons move the fastest towards the black hole's centre and slight perturbations to their trajectory owing to the error accumulated from numerical integration can render them unstable. But as $\alpha \rightarrow \frac{\pi}{2}$, the polar speed p^θ dominates the motion, and photons get dangerously close to the poles. Here as well, slight perturbations to the polar angle can render the trajectory unstable.

An ending note before we transition from ray tracing with analytically known metrics to numerical kinds and attempt to make shadows for hairy black holes as done in [11]: there are other approaches to solving the geodesic equations. In [2], Bacchini et al. decompose a metric into the $1 + 3$ form using the ADM formalism and evolve the kinematic variables with respect to the coordinate time t . The method of integration proposed is a Hamiltonian, implicit, iteration scheme that is computationally very expensive but produces stable trajectories for long integration times. This work was studied but not utilized here because only information about which part of the celestial sphere the photon intercepts is required for shadow production, and that too for many such photons. Hence a Runge-Kutta integrator suffices for this particular use case. In [35], Lora et al. compare the stability of different Runge-Kutta adaptive integrators and explain that the Dormand-Prince RK 4-5 Method is the best performer. The Cash-Karp RK 4-5 Method is used in this work because it was observed to conserve the Hamiltonian better than Dormand-Prince, and also requires lesser number of computations per step.

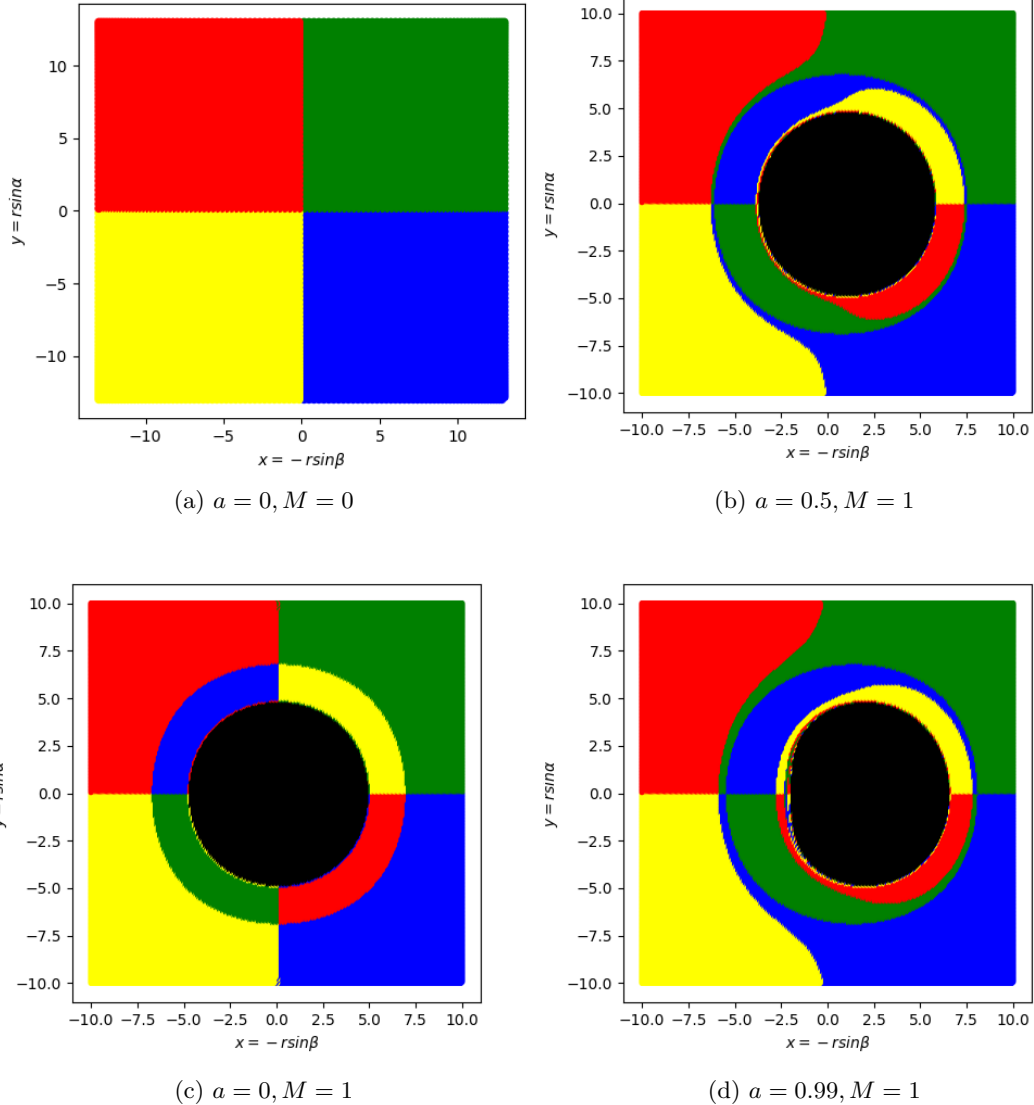


Figure 4.5: Reference of the flat spacetime background and shadows of Schwarzschild and Kerr black holes with a different value of the a parameter. 4.5a shows the trivial case that corresponds to Minkowski flat spacetime, where in photons travel in straight lines and the background appears unlensed. 4.5c is the shadow of a Schwarzschild blackhole, with the expected apparent horizon of $r \approx 5.196M$ and a concentric lensed region. 4.5b and 4.5d show shadows of Kerr black holes with different angular momentum. The Kerr black hole with $a = 0.99$ shows more frame dragging than the $a = 0.5$ model. All these images were made by backward integration of photons spread on a 250×250 screen till a final radial coordinate of $r = 15M$, the edge of the celestial sphere.

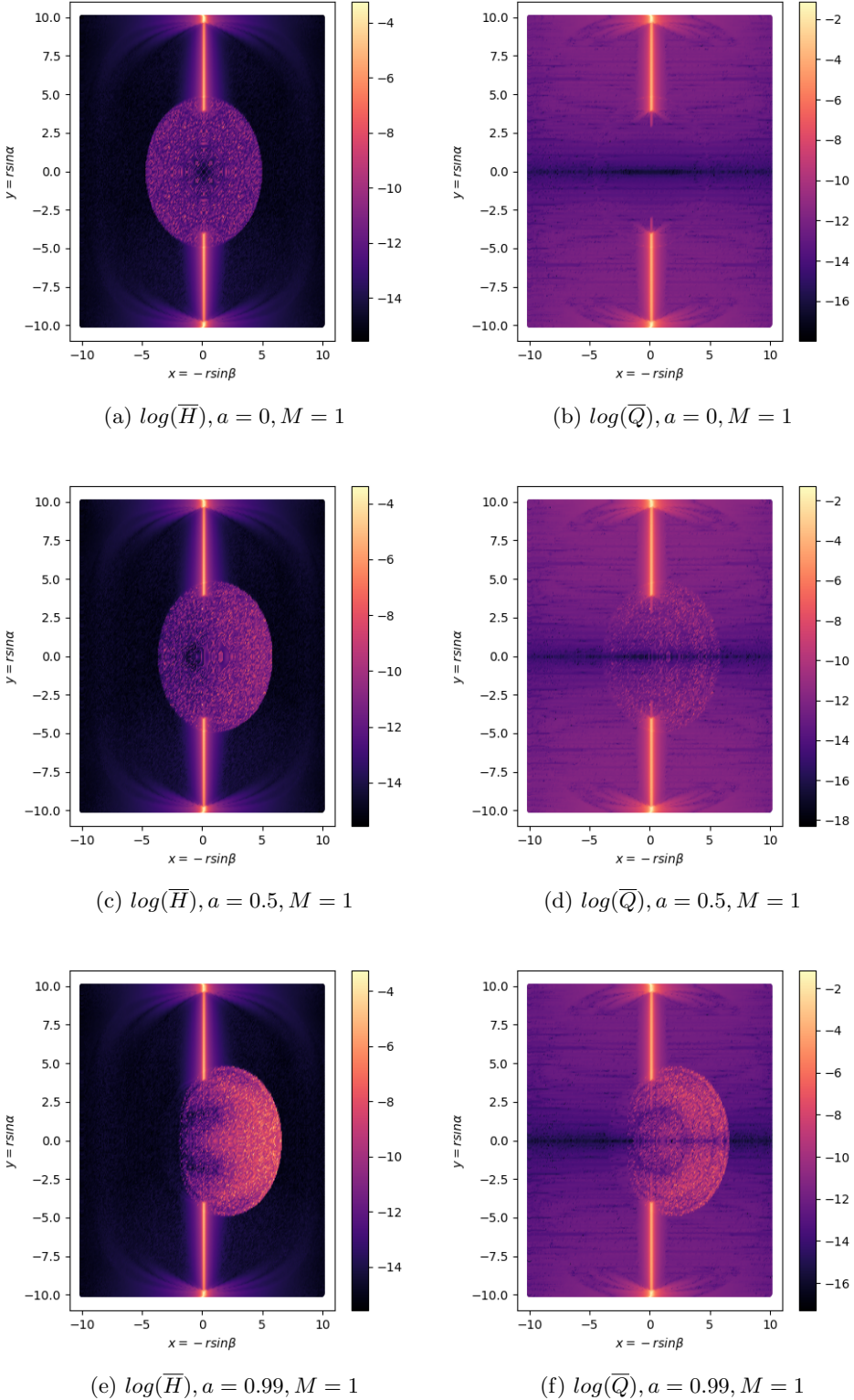


Figure 4.6: Deviation in the Hamiltonian \bar{H} and the Carter Constant \bar{Q} for the shadows discussed in Figure 4.5, shown in the log scale. Areas that produce the shadow, and the strip of photons that have zero angular momentum L are the most numerically challenging.

Chapter 5

Ray Tracing with Numerical Metrics

Chapter 4 dealt with developing a recipe to create a particle trajectory when the metric is given in analytical form. In contrast, metric solutions in modified theories of gravity are obtained numerically, so to use the equations of motion developed earlier, a method to continuously interpolate for a metric component or its derivative in the equations of motion must be developed. The numeric solutions depend on two variables, r and θ , so bicubic spline interpolation is the chosen method to obtain continuous values and is discussed first. Then to evaluate the effectiveness of this method in ray tracing, the Kerr solution is used as a test case.

5.1 Bicubic Spline Interpolation

The idea behind bicubic spline interpolation is simple. Given an arbitrary value of (x, y) that lies within a grid of (x_i, y_j) values, the task is to interpolate within the known discrete values of $f_{ij} = f(x_i, y_j)$ to extract the value of $f(x, y)$. To do so, four discrete values of the function are used, and these are the four nearest neighbours of the requested point (x, y) . The functional form used to fit for f is,

$$f(\bar{x}, \bar{y}) = \sum_{i=0}^3 \sum_{j=0}^3 a_{ij} \bar{x}^i \bar{y}^j, \quad (5.1)$$

where \bar{x}, \bar{y} are defined below as,

$$\bar{x} := \frac{x - x_0}{\Delta x}, \quad \bar{y} := \frac{y - y_0}{\Delta y}. \quad (5.2)$$

Given a requested point (x, y) , let us call the neighbouring points $(x_0, y_0), (x_0, y_1), (x_1, y_0), (x_1, y_1)$ which implies that the grid separation in the x and y directions are $\Delta x = x_1 - x_0$ and $\Delta y = y_1 - y_0$. These quantities define \bar{x} and \bar{y} in Equation (5.2), and these definitions ensure that \bar{x} and \bar{y} are normalized to lie between 0 and 1. To find the 16 coefficients a_{ij} , we make use of the values of the function at the four surrounding points, the values of the derivatives at these points in x and y , and lastly, the mixed derivatives at these points. To evaluate the derivatives, we make use of the following basic expressions given the ansatz in Equation (5.1).

$$f_x = \sum_{i=1}^3 \sum_{j=0}^3 \frac{a_{ij} i \bar{x}^{i-1} \bar{y}^j}{\Delta x}, \quad (5.3)$$

$$f_y = \sum_{i=0}^3 \sum_{j=1}^3 \frac{a_{ij} \bar{x}^i j \bar{y}^{j-1}}{\Delta y}, \quad (5.4)$$

$$f_{xy} = \sum_{i=1}^3 \sum_{j=1}^3 \frac{a_{ij} i \bar{x}^{i-1} j \bar{y}^{j-1}}{\Delta x \Delta y}. \quad (5.5)$$

It is not always guaranteed that these derivatives are available, and in most cases must be numerically computed. Given a location on the computational grid, numerically computing derivatives must be handled individually. In the cases their exists a point in front of and behind a grid point (or to the

left and to the right), a centered difference is used. These are found using a combination of Taylor's expansion as follows as shown below for the case of the x derivative.

$$f_{i+1,j} = f_{i,j} + f_x|_{i,j} \Delta x_1 + \frac{1}{2} f_{xx}|_{i,j} (\Delta x_1)^2 + \mathcal{O}(\Delta x_1)^3, \quad (5.6)$$

$$f_{i-1,j} = f_{i,j} - f_x|_{i,j} \Delta x_2 + \frac{1}{2} f_{xx}|_{i,j} (\Delta x_2)^2 - \mathcal{O}(\Delta x_2)^3. \quad (5.7)$$

Here Δx_1 is the step size in the forward direction equal to $x_{i+1} - x_i$, and Δx_2 is the step size in the backward direction equal to $x_i - x_{i-1}$. The right algebraic manipulation of the two above expressions gives the result,

$$f_x|_{i,j} = \frac{f_{i+1,j} \Delta x_2^2 - f_{i-1,j} \Delta x_1^2 - f_{i,j} (\Delta x_2^2 - \Delta x_1^2)}{\Delta x_1 \Delta x_2 (\Delta x_1 + \Delta x_2)} + \mathcal{O}(\Delta x_1 \Delta x_2). \quad (5.8)$$

In the case that the grid is uniformly spaced, the expression simplifies, and we have for the derivative in the x direction and analogously for y ,

$$f_x|_{(i,j)} = \frac{f_{i+1,j} - f_{i-1,j}}{2\Delta x} + \mathcal{O}(\Delta x)^2, \quad f_y|_{(i,j)} = \frac{f_{i,j+1} - f_{i,j-1}}{2\Delta y} + \mathcal{O}(\Delta y)^2. \quad (5.9)$$

For the case when there does not exist a neighbour in a given direction, we can still achieve second order accuracy in the derivatives by combining Taylor expansion's intelligently. Suppose we want to find the x derivative at a grid point which does not have any neighbours at a previous x location. In such a scenario, Taylor's expansion solely in the forward direction is used and we get,

$$f_{i+1,j} = f_{i,j} + f_x|_{i,j} \Delta x_1 + \frac{1}{2} f_{xx}|_{i,j} (\Delta x_1)^2 + \mathcal{O}(\Delta x_1)^3, \quad (5.10)$$

$$f_{i+2,j} = f_{i,j} + f_x|_{i,j} \Delta x_2 + \frac{1}{2} f_{xx}|_{i,j} (\Delta x_2)^2 + \mathcal{O}(\Delta x_2)^3. \quad (5.11)$$

Here $\Delta x_1 = x_{i+1} - x_i$, and $\Delta x_2 = x_{i+2} - x_i$. Again, correct algebraic manipulation yields that,

$$f_x|_{i,j} = \frac{f_{i+1,j} \Delta x_2^2 - f_{i+2,j} \Delta x_1^2 - f_{i,j} (\Delta x_2^2 - \Delta x_1^2)}{\Delta x_1 \Delta x_2 (\Delta x_2 - \Delta x_1)} + \mathcal{O}(\Delta x_1 \Delta x_2). \quad (5.12)$$

For a uniform grid, where $\Delta x_2 = 2\Delta x_1 = 2\Delta x$, we have for the derivative in the x direction, and analogously for y [40] that

$$f_x|_{(i,j)} = \frac{4f_{i+1,j} - f_{i+2,j} - 3f_{i,j}}{2\Delta x} + \mathcal{O}(\Delta x)^2, \quad f_y|_{(i,j)} = \frac{4f_{i,j+1} - f_{i,j+2} - 3f_{i,j}}{2\Delta y} + \mathcal{O}(\Delta y)^2. \quad (5.13)$$

Lastly, in the case there are no x points in front of a given grid point, we can solely do backward Taylor expansion to get,

$$f_{i-1,j} = f_{i,j} - f_x|_{i,j} \Delta x_1 + \frac{1}{2} f_{xx}|_{i,j} (\Delta x_1)^2 - \mathcal{O}(\Delta x_1)^3, \quad (5.14)$$

$$f_{i-2,j} = f_{i,j} - f_x|_{i,j} \Delta x_2 + \frac{1}{2} f_{xx}|_{i,j} (\Delta x_2)^2 - \mathcal{O}(\Delta x_2)^3. \quad (5.15)$$

Here $\Delta x_1 = x_i - x_{i-1}$, and $\Delta x_2 = x_i - x_{i-2}$. After algebraic manipulation we have,

$$f_x|_{i,j} = \frac{f_{i-1,j} \Delta x_2^2 - f_{i-2,j} \Delta x_1^2 - f_{i,j} (\Delta x_2^2 - \Delta x_1^2)}{\Delta x_1 \Delta x_2 (\Delta x_1 - \Delta x_2)} + \mathcal{O}(\Delta x_1 \Delta x_2). \quad (5.16)$$

For a uniform grid, where $\Delta x_2 = 2\Delta x_1 = 2\Delta x$, we have for the derivative in the x direction, and analogously for y that

$$f_x|_{(i,j)} = \frac{-4f_{i-1,j} + f_{i-2,j} + 3f_{i,j}}{2\Delta x} + \mathcal{O}(\Delta x)^2, \quad f_y|_{(i,j)} = \frac{-4f_{i,j-1} + f_{i,j-2} + 3f_{i,j}}{2\Delta y} + \mathcal{O}(\Delta y)^2. \quad (5.17)$$

The mixed derivative is performed by taking the x derivative of the y derivative, or vice versa. It is necessary to always be cognizant of how many points lie to the left, right, top and bottom of a given grid point. In this chapter, results in Kerr spacetime using the analytical metric will be compared to results using bicubic spline interpolation for the metric, using a uniform grid. In chapter 6, non-uniform data

from Collodel et al. is used for interpolation.

Now using the above prescription for the derivatives, one solves for the following set of equations. First, for the known function values we have,

$$f(0, 0) = a_{00}, \quad (5.18)$$

$$f(1, 0) = a_{00} + a_{10} + a_{20} + a_{30}, \quad (5.19)$$

$$f(0, 1) = a_{00} + a_{01} + a_{02} + a_{03}, \quad (5.20)$$

$$f(1, 1) = \sum_{i=0}^3 \sum_{j=0}^3 a_{ij}. \quad (5.21)$$

For the derivatives in x and y directions we get eight equations which are

$$\Delta x f_x(0, 0) = a_{10}, \quad (5.22)$$

$$\Delta x f_x(1, 0) = a_{10} + 2a_{20} + 3a_{30}, \quad (5.23)$$

$$\Delta x f_x(0, 1) = a_{10} + a_{11} + a_{12} + a_{13}, \quad (5.24)$$

$$\Delta x f_x(1, 1) = \sum_{i=1}^3 \sum_{j=0}^3 a_{ij} i, \quad (5.25)$$

$$\Delta y f_y(0, 0) = a_{01}, \quad (5.26)$$

$$\Delta y f_y(1, 0) = a_{01} + a_{11} + a_{21} + a_{31}, \quad (5.27)$$

$$\Delta y f_y(0, 1) = a_{01} + 2a_{02} + 3a_{03}, \quad (5.28)$$

$$\Delta y f_y(1, 1) = \sum_{i=0}^3 \sum_{j=1}^3 a_{ij} j. \quad (5.29)$$

Lastly, the four mixed derivatives give us the following

$$\Delta x \Delta y f_{xy}(0, 0) = a_{11}, \quad (5.30)$$

$$\Delta x \Delta y f_{xy}(1, 0) = a_{11} + 2a_{21} + 3a_{31}, \quad (5.31)$$

$$\Delta x \Delta y f_{xy}(0, 1) = a_{11} + 2a_{12} + 3a_{13}, \quad (5.32)$$

$$\Delta x \Delta y f_{xy}(1, 1) = \sum_{i=1}^3 \sum_{j=1}^3 a_{ij} ij. \quad (5.33)$$

The expressions are greatly simplified by normalizing \bar{x}, \bar{y} to lie between 0 and 1. One can write these 16 equations in matrix form and invert to solve for the 16 unknowns a_{ij} . The final expressions for these coefficients are as given below in the form $A = XYZ$, with

$$A = \begin{pmatrix} a_{00} & a_{01} & a_{02} & a_{03} \\ a_{10} & a_{11} & a_{12} & a_{13} \\ a_{20} & a_{21} & a_{22} & a_{23} \\ a_{30} & a_{31} & a_{32} & a_{33} \end{pmatrix}, \quad X = \begin{pmatrix} 1 & 0 & 0 & 0 \\ 0 & 0 & 1 & 0 \\ -3 & 3 & -2 & -1 \\ 2 & -2 & 1 & 1 \end{pmatrix} \quad (5.34)$$

$$Y = \begin{pmatrix} f(0, 0) & f(0, 1) & \Delta y f_y(0, 0) & \Delta y f_y(0, 1) \\ f(1, 0) & f(1, 1) & \Delta y f_y(1, 0) & \Delta y f_y(1, 1) \\ \Delta x f_x(0, 0) & \Delta x f_x(0, 1) & \Delta x \Delta y f_{xy}(0, 0) & \Delta x \Delta y f_{xy}(0, 1) \\ \Delta x f_x(1, 0) & \Delta x f_x(1, 1) & \Delta x \Delta y f_{xy}(1, 0) & \Delta x \Delta y f_{xy}(1, 1) \end{pmatrix}, \quad Z = \begin{pmatrix} 1 & 0 & -3 & 2 \\ 0 & 0 & 3 & -2 \\ 0 & 1 & -2 & 1 \\ 0 & 0 & -1 & 1 \end{pmatrix} \quad (5.35)$$

5.2 Recipe and Comparison with a Kerr Black Hole

Bicubic spline interpolation was used to trace trajectories in a Kerr spacetime with $M = 1, a = 0.5$. The steps used are outlined below:

- Create a class *stationary axisymmetric data* that stores the discrete data points and interpolates for them within a fixed grid. Initialize the class with the mass of the black hole, angular momentum per unit mass a , the number of points in x called *xsize*, the number of points in y called *ysize*, the uniform x separation *dx* and the uniform y separation *dy*. Create an empty two-dimensional array called *data* that will store the values of the metric and its derivatives at all the discrete points where they are known, and an empty three dimensional array *coeff* that will store the values of the 16 spline coefficients in each cell, found by solving for the ansatz in Equation (5.1).
- Fill the *data* array with all the values of the 5 metric terms and their 10 derivatives required to integrate the equations of motion as outlined in Chapter 4. The first two rows should store the x and y points respectively, making *data* an array of shape $17 \times (\text{xsize} * \text{ysize})$.
- In preparation for locating the four nearest neighbours of a requested point (x, y) , prepare a function called *sorter* which locates the point smallest in both their coordinates out of the four nearest neighbours. For a uniform grid this is done simply by,

$$i = \text{int}\left(\frac{x - \text{data}[0][0]}{\text{dx}}\right), \quad j = \text{int}\left(\frac{y - \text{data}[1][0]}{\text{dy}}\right), \quad I = i * \text{ysize} + j, \quad (5.36)$$

where I is the index of the smallest coordinate value neighbour. The convention followed is *data* is populated by first fixing x , sampling through all values of y , and then marching to the next x value. *data[0][0]* is the smallest value of x in the grid and *data[1][0]* is the smallest value of y in the grid.

- Write functions *diff_x*, *diff_y* and *diff_{xy}* that take two numbers as input, one the index of the grid point, and the second is the serial number of the function being differentiated. For example, to calculate the r derivative of the term g_{tt} at a given value of (r, θ) , we call *diff_x(n₁, n₂)* where *n₁* is the location of (r, θ) in the grid and *n₂* is the serial number of the term g_{tt} , both with respect to the array *data* which was populated before.
- Write a function *bicubic spline coeff* which calculates the 16 spline coefficients in each cell. To do this, loop over every grid point, dropping those points that do not classify as possible neighbours that would have the smallest coordinates given a request point. (These are points that either have the biggest value of x or y in the data set or both at the same time.) For those points that do qualify, treat them as potential points with smallest coordinates out of all four neighbours and calculate the spline coefficient using the formulae provided. Store these in the three dimensional array *coeff* declared before. *coeff* is an array with shape $15 \times (\text{xsize} * \text{ysize}) \times 16$. (15 instead of 17 because now there is no need to store the (x, y) values as we abandon points and care about cells now.) Call this function now so that all coefficients are calculated in each cell before ray tracing begins.
- Write a final function *bicubic spline* that takes the same number and types of input as the previous function *diff_x* and returns the value of a function by combining the coefficients found in the previous step, using Equation (5.1).
- As the particle moves around in (r, θ) , the equations of motion must be supplied values of the metric and its derivatives at these points. So, in the necessary functions that integrate the equations of motion, include a new variable *index* which is equal to the neighbour with the smallest coordinates. This is nothing but the return value of the *sorter* function which should be called each time the particle moves to a new (r, θ) . Enter *index* into the *bicubic spline* function to supply the value of the required metric/derivative of the metric term in the equations of motion.
- While using the preferred numerical integrator, check to see if the particle exits the grid at any point. If so, terminate integration.
- Perform the same error analysis with Carter Constant and \bar{H} as done before.

The error now is dictated by the accuracy of the bicubic spline interpolation, and it is not realistic to expect the same amount of accuracy as was experienced before with pure analytical ray tracing. To see the viability of bicubic spline interpolation for dealing with numerical metrics, an error analysis was performed. Splines were constructed using the recipe above for $M = 1$ and $a = 0.5$. A Kerr black hole with these properties possesses an outer event horizon of $r_+ = 1.866$. So the array *data* was populated with 1000 r values ranging from $r = 1.96$ to $r = 100.1$, 100 θ values ranging from $\theta = 0$ to $\theta = \pi$ and the values of the metric terms and their derivatives ∂_r and ∂_θ . The accuracy of the spline can potentially be improved by sampling more r values.

In principle, one can fit for the metric terms and their derivatives directly, but a cleaner way is to fit functional forms that do not possess divergences. For example, instead of fitting the metric term $g_{rr} = \frac{\Sigma}{\Delta}$ directly, it is better to fit for $\widetilde{g_{rr}} = g_{rr}\Delta - r^2 = a^2 \cos^2\theta$. This avoids the singularity of Δ near r_+ and the rapid growth of Σ at large values of r . The real value of g_{rr} can easily be recovered from $\widetilde{g_{rr}}$ by an inversion at the final step of spline interpolation, in the function *bicubic spline*. After assessing all the potential problems in the five metric terms and their derivatives, nine of them were fit directly, where as six of them were modified as follows,

$$\widetilde{g_{rr}} = g_{rr}\Delta - r^2 = a^2 \cos^2\theta, \quad (5.37)$$

$$\widetilde{g_{\theta\theta}} = g_{\theta\theta} - r^2 = a^2 \cos^2\theta, \quad (5.38)$$

$$\widetilde{g_{\phi\phi}} = g_{\phi\phi} - r^2 \sin^2\theta = \left(a^2 + \frac{r_s r a^2}{\Sigma} \sin^2\theta \right) \sin^2\theta, \quad (5.39)$$

$$\widetilde{\partial_\theta g_{rr}} = \partial_\theta g_{rr}\Delta = -a^2 \sin 2\theta, \quad (5.40)$$

$$\widetilde{\partial_r g_{rr}} = \partial_r g_{rr}\Delta^2 = 2(r\Delta - (r - M)\Sigma), \quad (5.41)$$

$$\widetilde{\partial_\theta g_{\phi\phi}} = \partial_\theta g_{\phi\phi} - r^2 \sin 2\theta = \left(a^2 + \frac{r_s r a^2 \sin^2\theta}{\Sigma} \right) \sin 2\theta + \frac{2m r a^2 \sin^2\theta \sin 2\theta (\Sigma + a^2 \sin^2\theta)}{\Sigma^2}. \quad (5.42)$$

These manipulations avoid the divergence of Δ at $r = r_+$ and also as r gets very large. Any further manipulation would be too cosmetic, so it is avoided entirely. To ascertain the effectiveness of the created splines, 10,000 points evenly spaced out in the $r - \theta$ domain were sampled and the relative errors between the spline value and the analytical result were plotted in Figures 5.1, 5.2 and 5.3 in the log scale. The convention of relative error used was equal to,

$$\Delta f = \frac{|f_{\text{spline}} - f_{\text{analytical}}|}{f_{\text{analytical}}}. \quad (5.43)$$

The highest relative error was on the order of 10^{-3} , whereas the term $\partial_r g_{\theta\theta} = 2r$ was identically zero everywhere in the test $r - \theta$ space and its plot is not presented. The exceptional performance of $\partial_r g_{\theta\theta}$ is explained by the linear dependence of $\partial_r g_{\theta\theta}$ on r , so the bicubic polynomial fits the function to numerically perfect accuracy. In all of the plots, the relative error starts to get larger at the horizon or at the poles.

Figure 5.4 compares the analytically generated shadows from Chapter 4 to their spline counterparts. To the naked eye, they appear completely identical; Out of 62,500 pixels, there were 32 cases of difference in the Schwarzschild case, 4 cases of difference in the Kerr case with $a = 0.5$, and 6 cases of difference in the Kerr case with $a = 0.99$. This signals the victory of bicubic spline interpolation as a method to produce a lensed background using a numerical metric. Figure 5.5 shows the deviation of the Hamiltonian and the Carter Constant for the spline-produced shadows. Again, numerical difficulties lie in the shadow region's rim, and the vertical strip which consists of $L = 0$ photons.

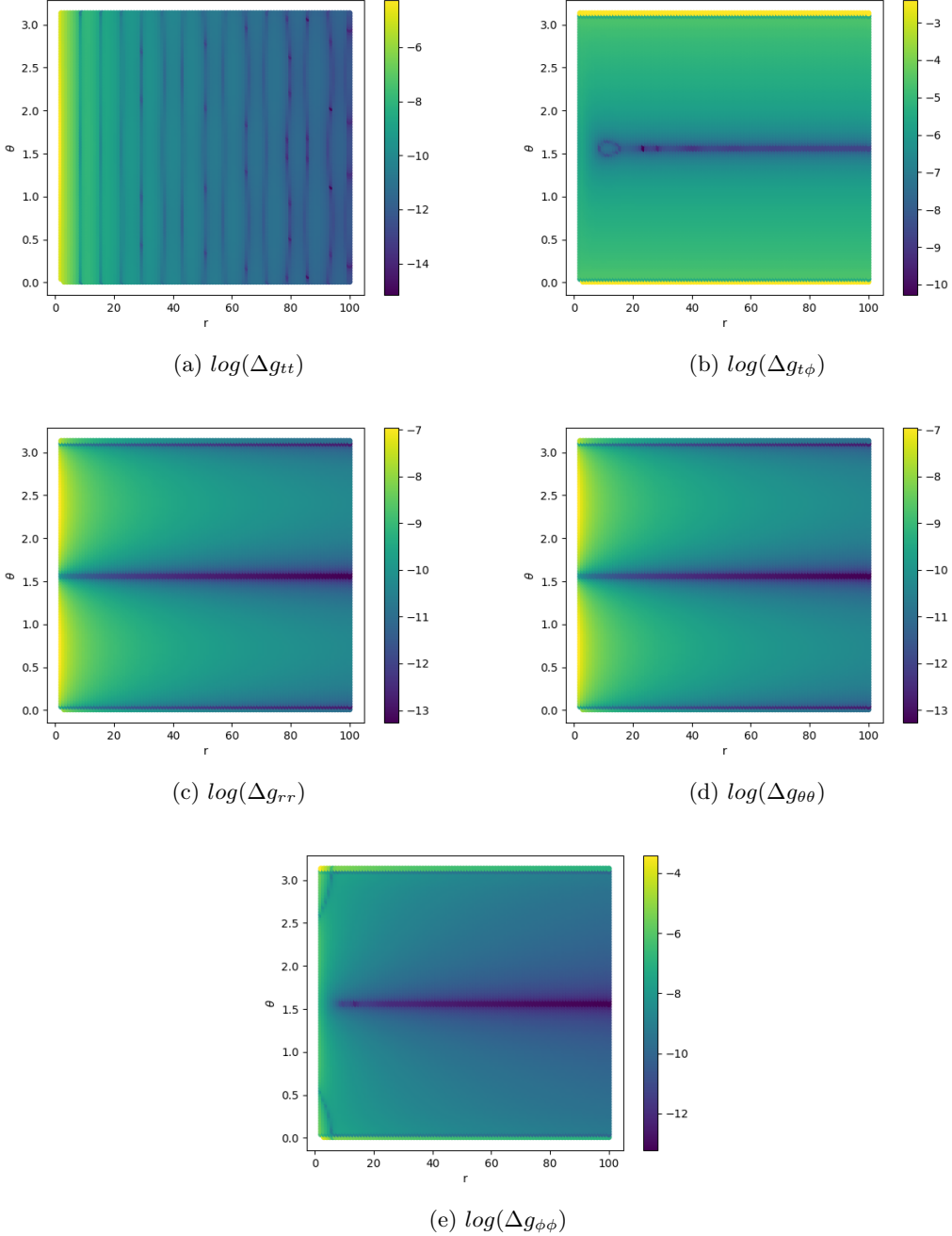


Figure 5.1: Errors in bicubic spline interpolation for the 5 metric terms $g_{tt}, g_{t\phi}, g_{rr}, g_{\theta\theta}, g_{\phi\phi}$. 1000 points in r and 100 points in θ were taken to construct the splines. Then, 10,000 points evenly spaced out in r and θ were sampled and the relative deviation of the 5 metric terms at these points was plotted. It is observed that fitting functional forms that avoid divergences have reduced error and the highest deviations in most cases occur close to the event horizon or at the poles.

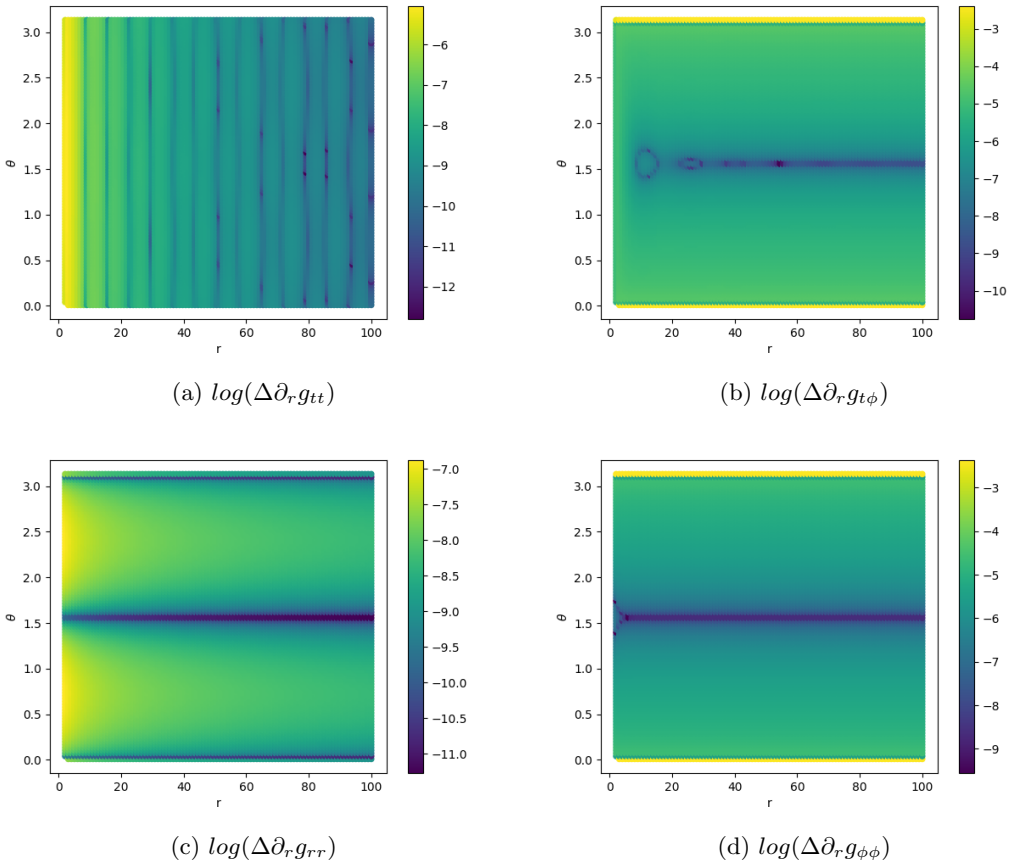


Figure 5.2: Errors in bicubic spline interpolation for the ∂_r derivatives of the 4 metric terms, $g_{tt}, g_{t\phi}, g_{rr}, g_{\phi\phi}$. 1000 points in r and 100 points in θ were taken to construct the splines. Then, 10,000 points evenly spaced out in r and θ were sampled and the deviation of the r derivative of the 5 metric terms at these points was plotted. It is observed that fitting functional forms that avoid divergences have reduced error and the highest deviations in most cases occur close to the event horizon or at the poles. The situation for $\partial_r g_{\theta\theta}$ is trivial, as the simplified form renders the bicubic polynomial fit perfectly accurate.

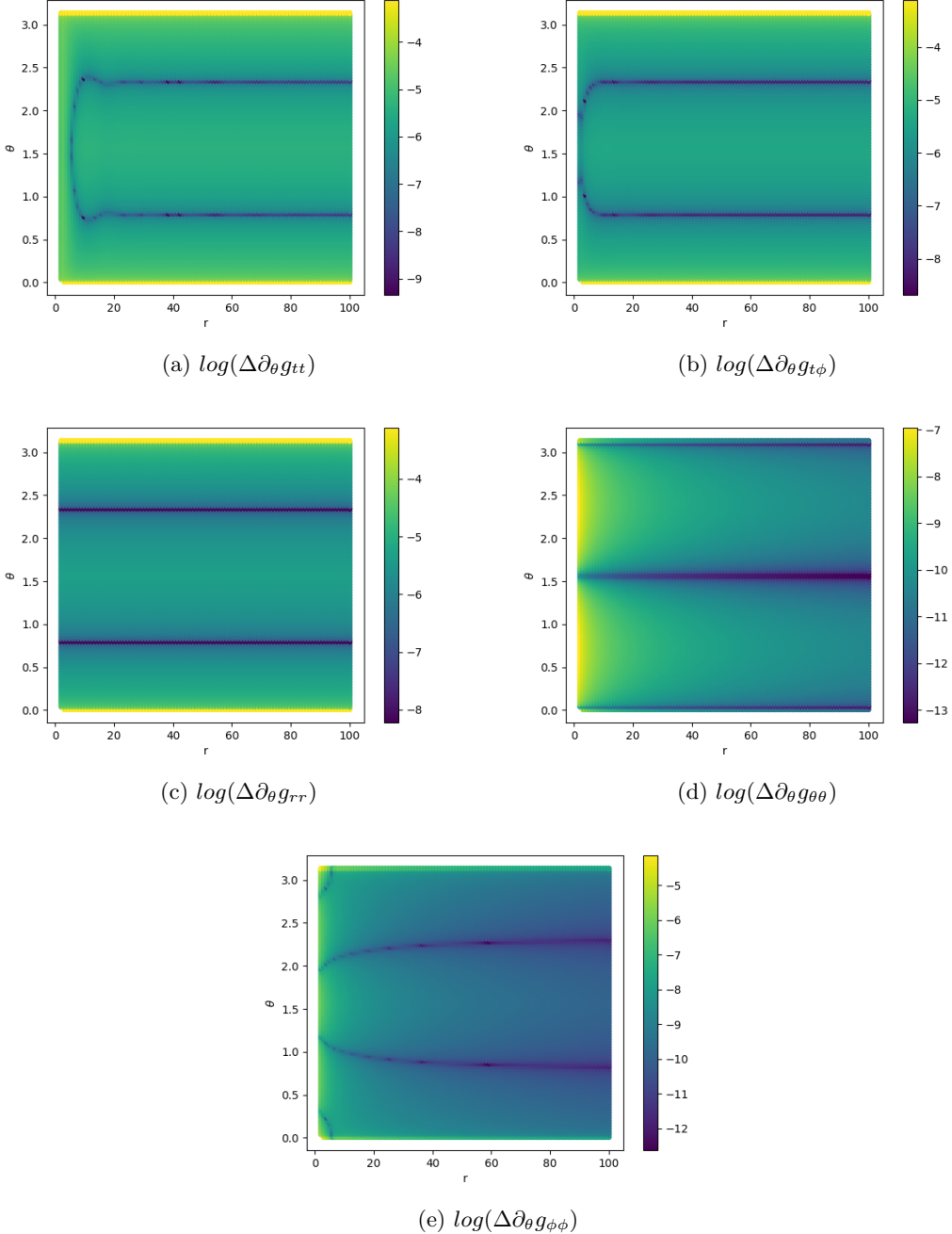


Figure 5.3: Errors in bicubic spline interpolation for the ∂_θ derivatives of the 5 metric terms, $g_{tt}, g_{t\phi}, g_{rr}, g_{\theta\theta}, g_{\phi\phi}$. 1000 points in r and 100 points in θ were taken to construct the splines. Then, 10,000 points evenly spaced out in r and θ were sampled and the deviation of the θ derivative of the 5 metric terms at these points was plotted. It is observed that fitting functional forms that avoid divergences have reduced error and the highest deviations occur close to the event horizon or at the poles.

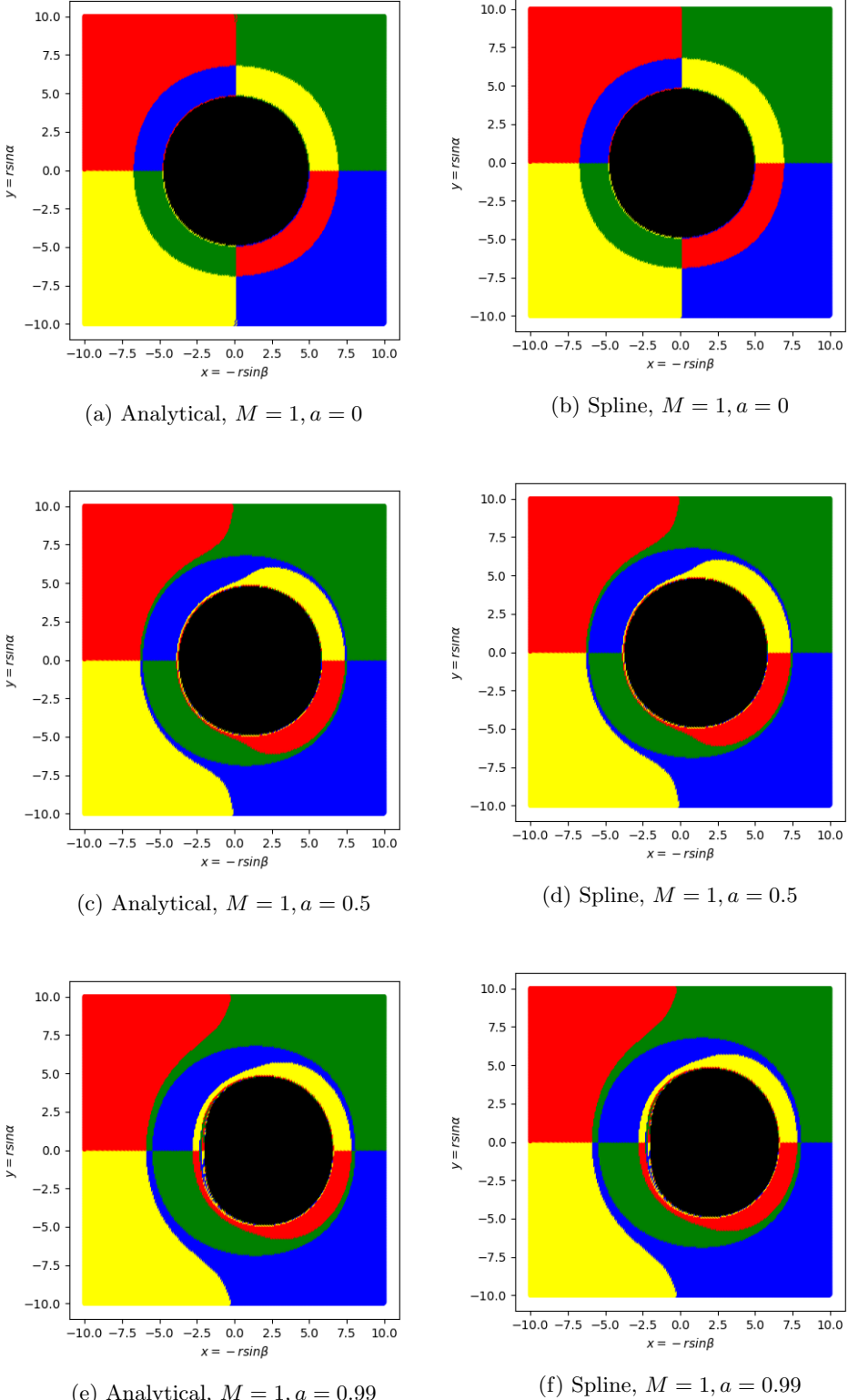


Figure 5.4: Comparison between analytical and spline results for the shadow of a Kerr black hole with $M = 1, a = 0, 0.5, 0.99$ for an observer located at $(r = 15M, \theta = \frac{\pi}{2}, \phi = 0)$. Out of 62,500 pixels, the Schwarzschild shadow had 32 deviant pixels, the Kerr shadow with $a = 0.5$ had 4 deviant pixels, and the Kerr shadow with $a = 0.99$ had 6 deviant pixels.

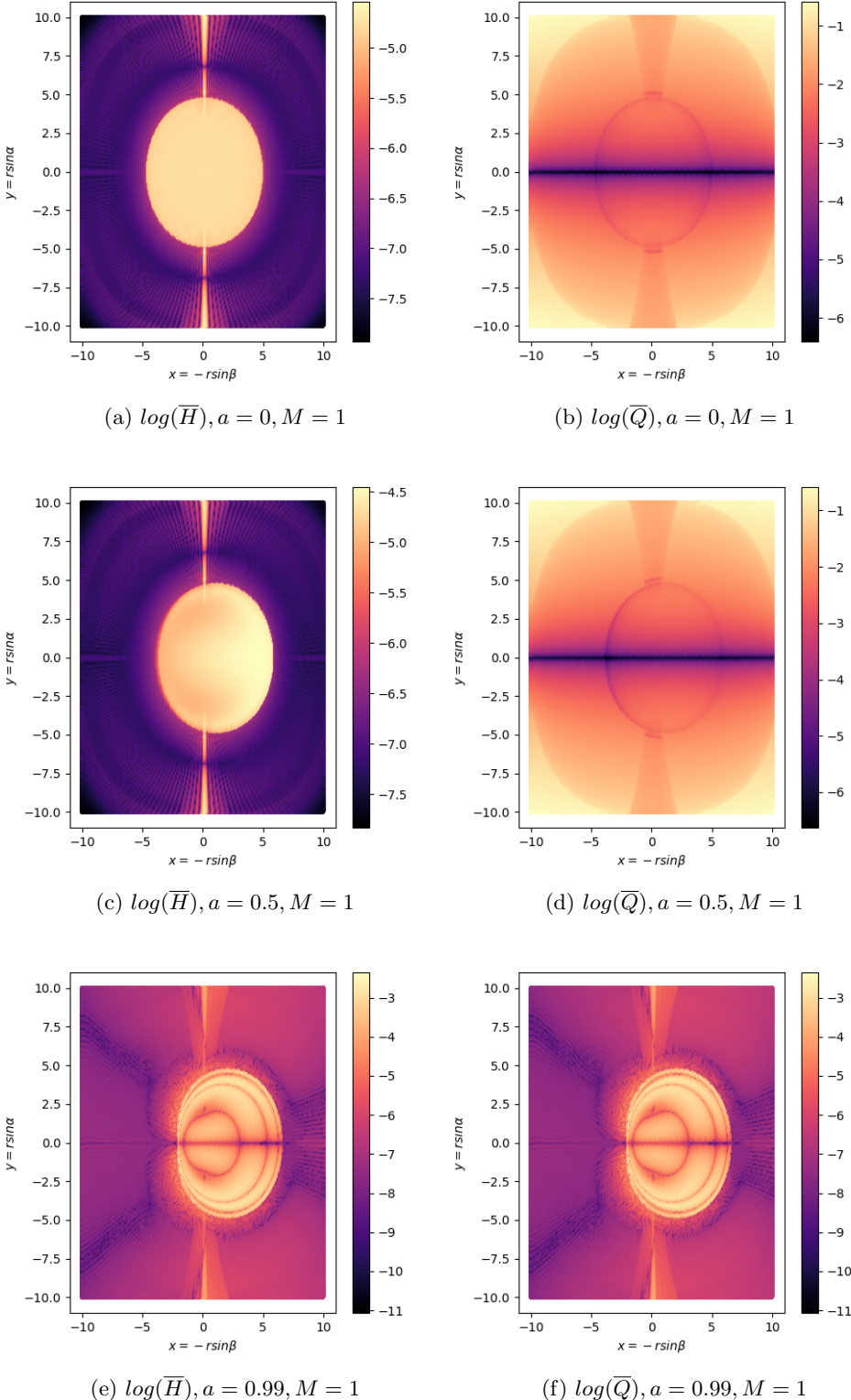


Figure 5.5: Deviation in the Hamiltonian \bar{H} and the Carter Constant \bar{Q} for the spline-constructed shadows discussed in Figure 5.4, shown in the log scale. Areas that produce the shadow, and the strip of photons that have zero angular momentum L are the most numerically challenging.

Chapter 6

Results for KBHSH

We are now ready to trace trajectories of photons in the spacetime solutions of two-scalar field theories of gravity, found by Collodel et al. in [9]. Starting with a brief list of changes and modifications compared to ray tracing in Kerr spacetime, a comparison with cloud solutions in two-scalar field theory is made, with the expectation that rays behave similarly to their Kerr counterparts. The chapter ends with a discussion of numerical challenges in certain settings, and further scope for improvement in the ray tracing code.

6.1 Modified Recipe for Ray Tracing

Below is the list of changes to the ray tracing algorithm developed in Chapters 4 and 5

- With a stationary and axisymmetric line element of the form given in Equation (2.30), repeated below for convenience.

$$ds^2 = (-\mathcal{N}e^{2F_0} + e^{2F_2}\omega^2 \sin^2\theta) dt^2 - 2e^{2F_2}r\omega \sin^2\theta dt d\phi + \frac{e^{2F_1}}{\mathcal{N}} dr^2 + e^{2F_1}r^2 d\theta^2 + e^{2F_2}r^2 \sin^2\theta d\phi^2. \quad (6.1)$$

The equations of motion to be integrated numerically stay as in Equations (3.51), (3.52), (4.21) and (4.22). The explicit forms of the derivatives of the metric are now modified as below,

$$\partial_\theta g_{rr} = \frac{r}{r - r_h} \cdot e^{2F_1} \cdot 2\partial_\theta F_1, \quad (6.2)$$

$$\partial_r g_{rr} = -e^{2F_1} \frac{r_h}{(r - r_h)^2} + \frac{r}{r - r_h} e^{2F_1} \cdot 2\partial_r F_1, \quad (6.3)$$

$$\partial_r g_{tt} = -e^{2F_0} \frac{r_h}{r^2} - \left(1 - \frac{r_h}{r}\right) e^{2F_0} \cdot 2\partial_r F_0 + \sin^2\theta (2\omega\partial_r \omega e^{2F_2} + \omega^2 e^{2F_2} \cdot 2\partial_r F_2), \quad (6.4)$$

$$\partial_r g_{t\phi} = -\omega \sin^2\theta e^{2F_2} - \partial_r \omega r \sin^2\theta e^{2F_2} - \omega r \sin^2\theta e^{2F_2} \cdot 2\partial_r F_2, \quad (6.5)$$

$$\partial_r g_{\theta\theta} = 2r e^{2F_1} + r^2 e^{2F_1} \cdot 2\partial_r F_1, \quad (6.6)$$

$$\partial_r g_{\phi\phi} = 2r \sin^2\theta e^{2F_2} + r^2 \sin^2\theta e^{2F_2} \cdot 2\partial_r F_2, \quad (6.7)$$

$$\partial_\theta g_{tt} = -\left(1 - \frac{r_h}{r}\right) e^{2F_0} \cdot 2\partial_\theta F_0 + \sin^2\theta e^{2F_2} \omega^2 + \sin^2\theta (2\omega\partial_\theta \omega e^{2F_2} + \omega^2 e^{2F_2} \cdot 2\partial_\theta F_2), \quad (6.8)$$

$$\partial_\theta g_{t\phi} = -\partial_\theta \omega r \sin^2\theta e^{2F_2} - \omega r \sin^2\theta e^{2F_2} - \omega r \sin^2\theta e^{2F_2} \cdot 2\partial_\theta F_2, \quad (6.9)$$

$$\partial_\theta g_{\theta\theta} = r^2 e^{2F_1} \cdot 2\partial_\theta F_1, \quad (6.10)$$

$$\partial_\theta g_{\phi\phi} = r^2 \sin^2\theta e^{2F_2} + r^2 \sin^2\theta e^{2F_2} \cdot 2\partial_\theta F_2. \quad (6.11)$$

- The data file provided is a solution to the two-scalar field gravity field equations for a specified r_h and ω_s . To use the same adaptive time stepping based on the radial coordinate r in terms of the mass of the compact object, an external script¹ was used to ascertain the ADM mass and angular momentum.
- Instead of creating a spline from analytically-known functions as in Chapter 5, data will be read directly from a file. Now in the class *stationary axisymmetric data*, the *data* array will store just $x, \theta, F_0, F_1, F_2, \omega$ and be of dimension $6 \times (xsize * ysize)$. Similarly, *coeff* is now a $4 \times (xsize * ysize) \times 16$ array. The files typically have 120 points in the compactified radial coordinate x and 30 points in the polar coordinate $\theta \in [0, \frac{\pi}{2}]$.
- The separation in x and θ is not uniform, so the *sorter* function can't trivially locate the index of the smallest coordinate neighbour. In this scenario, each value of the x and θ coordinate should be checked to see the smallest positive values of the expressions,

$$\delta x = x - x_i, \quad i \in [0, 119], \quad (6.12)$$

$$\delta\theta = \theta - \theta_j, \quad j \in [0, 29]. \quad (6.13)$$

The search can be terminated when the above expressions turn negative. Since this time *data* is populated for all values of x for a fixed θ before marching to the next value of θ , the index of the smallest coordinate neighbour is given by $I = j * xsize + i$.

- A request point (r, θ) must be converted to (x, θ) for the *sorter* function. The definition of $x(r)$ is repeated below,

$$x = \frac{\sqrt{r^2 - r_h^2}}{\sqrt{r^2 - r_h^2} + 1}. \quad (6.14)$$

Also, since reflection symmetry of the metric is assumed about the equatorial plane, for $\frac{\pi}{2} < \theta \leq \pi$, one must set $\theta \rightarrow \pi - \theta$ before using the search algorithm.

- The functions *sorter*, *diff_x*, *diff_y* and *diff_{xy}* now must also accommodate for a non-uniform grid, in case they used the uniform grid expressions from before.
- Since the equations of motion require the derivatives of F_0, F_1, F_2, ω in the $r - \theta$ directions, we will also write two more functions *bicubic spline diff x* and *bicubic spline diff y* that will return the derivatives in x and y of the ansatz in Equation (5.1). Again, θ must be adjusted if it lies in the range $\frac{\pi}{2} < \theta \leq \pi$. Since the spline fits for the compactified radial coordinate x , to find $\partial_r f$ we can write,

$$\partial_r f = \frac{\partial f}{\partial x} \frac{\partial x}{\partial r}, \quad \frac{\partial x}{\partial r} = \frac{r}{\sqrt{r^2 - r_h^2} \left(\sqrt{r^2 - r_h^2} + 1 \right)^2}. \quad (6.15)$$

- Now in the subroutine that integrates the equations of motion, use the generated splines to evaluate $F_0, F_1, F_2, \omega, \partial_r F_0, \partial_r F_1, \partial_r F_2, \partial_r \omega, \partial_\theta F_0, \partial_\theta F_1, \partial_\theta F_2, \partial_\theta \omega$ every time the particle moves to a new (r, θ) coordinate.
- Since there is no Carter Constant for general stationary and axisymmetric space times, restrict the error analysis to \bar{H} .

6.2 Comparison of Cloud Shadows with Kerr Counterparts

The solutions found by Collodel et al. have a numerical accuracy on the order of $10^{-3} - 10^{-4}$. To ascertain whether or not it is feasible to interpolate for this data and produce a realistic shadow, comparisons are made for cloud solutions with Kerr counterparts. The expectation is that up to some numerical accuracy, the shadows should coincide.

The Boyer-Lindquist coordinates are different than the coordinates in which numerical solutions for KBSH were found in [9]. For a good comparison, the technique developed in [12] is followed, where the circumferential radius, equal to $r_0 = \sqrt{g_{\phi\phi}}|_{\theta=\frac{\pi}{2}}$ is taken to be the same at the location of the observer in both coordinates. In this work, the observer was placed at $r = 15M$ in the coordinates of [9]. This sets a value for $g_{\phi\phi}$, which is used to work out the radial location in the Boyer Lindquist coordinate system.

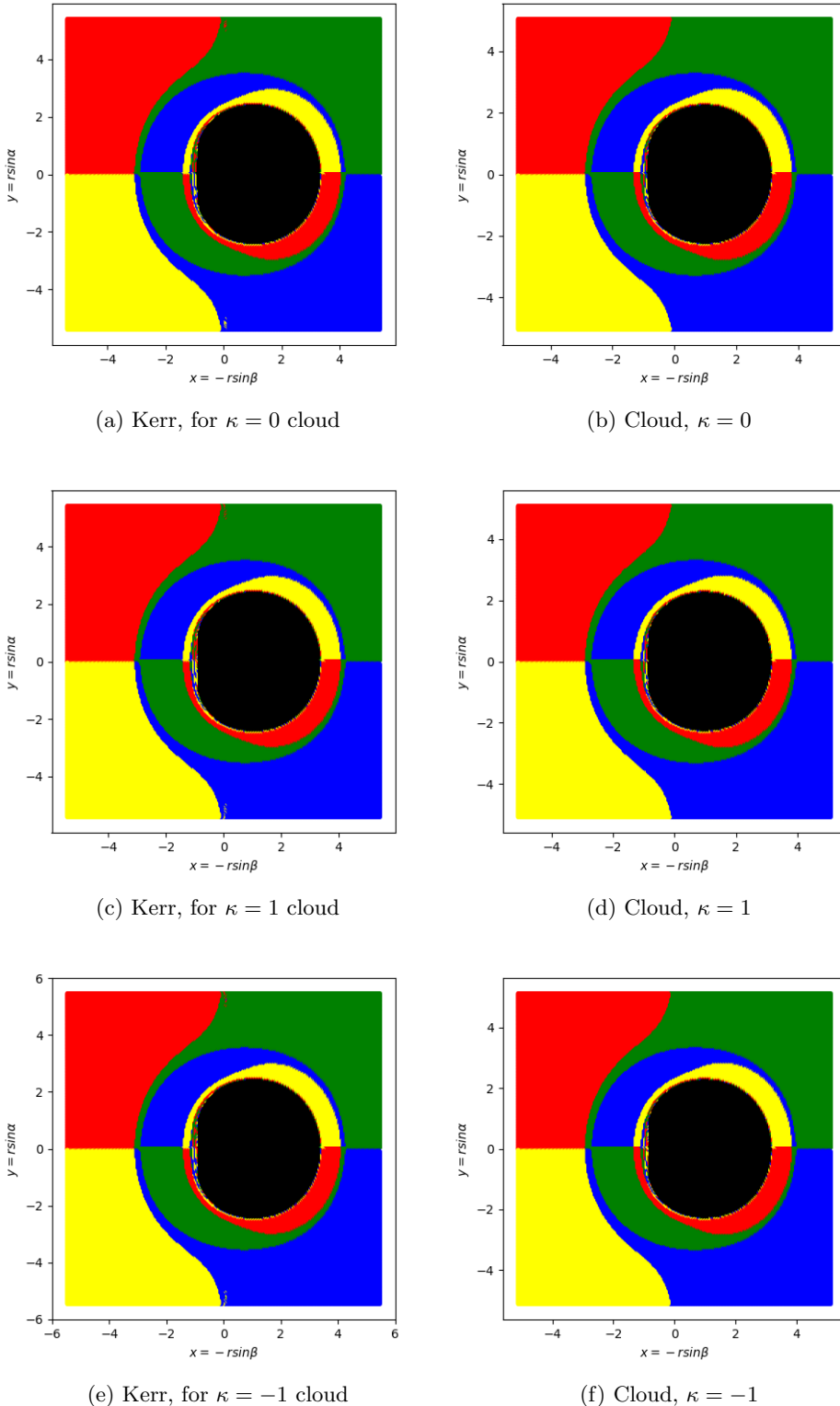


Figure 6.1: Comparison between the shadows of numerical cloud solutions from two-scalar field theory and the corresponding Kerr black hole with the same ADM masses, for $\kappa = 0, 1, -1$ for an observer located at $(r = 15M, \theta = \frac{\pi}{2}, \phi = 0)$. Due to the difference in coordinate systems, the observer in the Kerr situation was placed at the same circumferential radius. The horizon areas were compared and found to coincide up to the fourth decimal place as seen in Table 6.1.

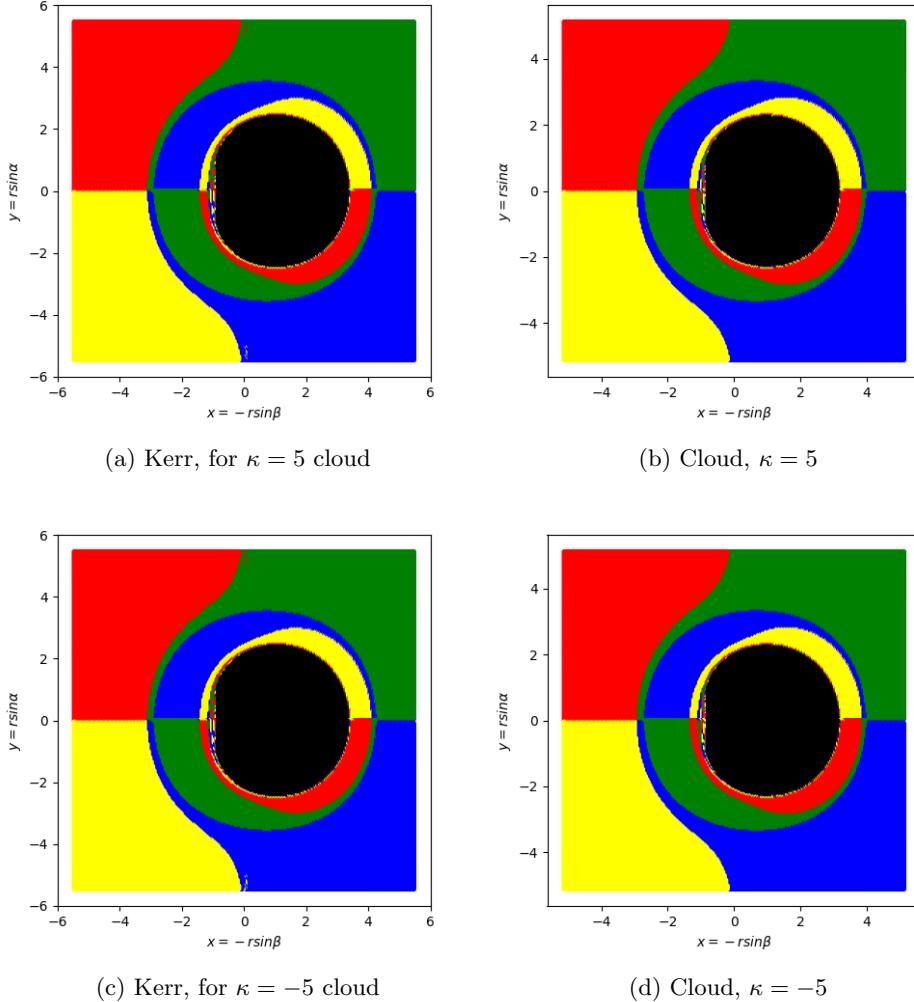


Figure 6.2: Comparison between the shadows of numerical cloud solutions from two-scalar field theory and the corresponding Kerr black hole with the same ADM masses, for $\kappa = 5, -5$ for an observer located at $(r = 15M, \theta = \frac{\pi}{2}, \phi = 0)$. Due to the difference in coordinate systems, the observer in the Kerr situation was placed at the same circumferential radius. The horizon area was found to coincide up till the fourth decimal place as seen in Table 6.1.

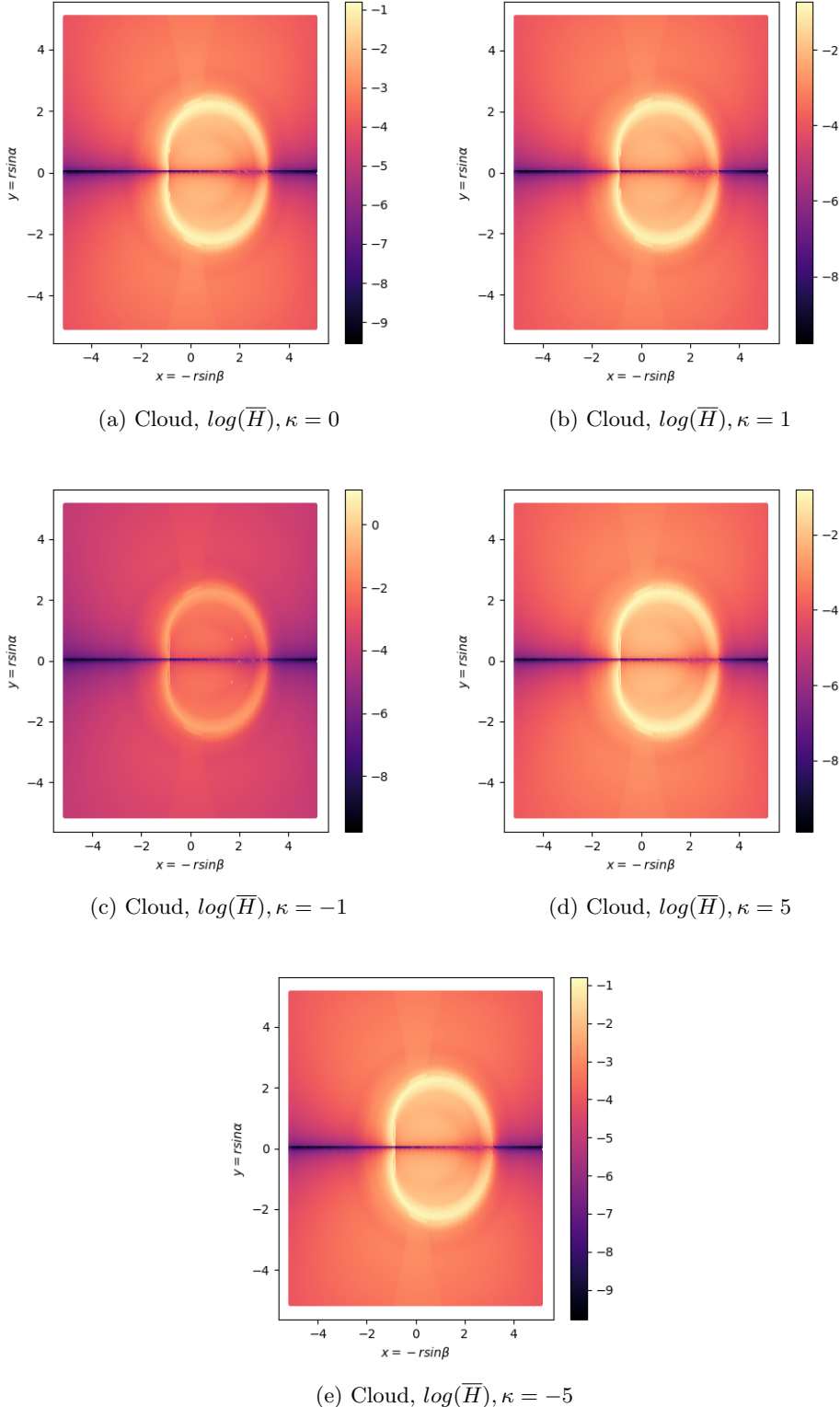


Figure 6.3: Deviation in the Hamiltonian \bar{H} for the shadows of numerical cloud solutions in two-scalar field theory of gravity, shown in the second column of Figures 6.1 and 6.2; the average Hamiltonian is shown in the log scale. Areas close to the rim of the shadow produce the most error.

Figures 6.1 and 6.2 display the shadows of cloud solutions from [9], versus their Kerr counterparts. All the cases $\kappa = 0, 1, -1, 5, -5$ discussed in the paper were explored. To the naked eye, the shadows look alike confirming that it is possible to use numerical metrics of a given accuracy, alongside bicubic spline interpolation and a geodesic integrator to produce acceptable shadows. As expected, the average deviation of the Hamiltonian shown in the log scale in Figure 6.3 is higher than in Figures 4.6 and 5.5. The numeric quality of the metric of a given accuracy limits the overall performance of the spline interpolation and consequent geodesic integration. Photons that come close to the edge of the horizon and experience strong deflections showcase maximum error.

To quantitatively understand the coincidence of the numerical cloud solutions with their Kerr counterparts, the horizon area was calculated, simply by dividing the frequency of black pixels to the total number of pixels, which was a fixed 62,500 in each case. The results are shown in Table 6.1, alongside the ADM mass and angular momentum for each configuration. It can be seen that the horizon areas coincide up to the fourth decimal place, signifying that accurate shadows were produced for the numerical cloud solutions.

κ	M	J	Kerr HA	Cloud HA
0	0.504	0.254	0.1272	0.1271
1	0.508	0.258	0.1268	0.1268
-1	0.511	0.259	0.1267	0.1264
5	0.512	0.262	0.1267	0.1264
-5	0.512	0.262	0.1268	0.1264

Table 6.1: Comparison of Cloud and Kerr Horizon Area

6.3 Chaotic Shadows and Future Work

The handwritten bicubic spline interpolation routine and integrator managed to produce the shadow of numerical cloud solutions. These solutions look like Kerr shadows, with a dragged lensed background and a D-like shadow. As was shown in [11], the shadows of KBHSH with an increasing amount of scalar field contribution have smaller shadows, with a chaotic lensing structure. This is also seen with a few test solutions with heavy hair found by Collodel et al. shown in in Figure 6.4. In all the plots, what would have otherwise been a central dark region is replaced by few disconnected dark spots, which are called eyebrows in the work by Cunha et al. in [12]. Around these dark spots we see a chaotic lensed region, which is created by photon geodesics exhibiting complicated trajectories within this impact parameter region.

The left column in Figure 6.4 shows results from the handwritten code based on previous formalism of this thesis, where as the right column shows independent results² which capture the chaotic structure to better resolution. The handwritten geodesic integrator based on the Cash-Karp explicit Runge Kutta method used throughout this thesis work struggles to re-produce the exact chaotic lensed region. It is observed that trajectories which contribute to this chaotic lensed region approach close to the event horizon at about $r \approx 10r_h$, and perform complicated oscillatory trajectories before moving towards the edge of the computational celestial sphere. To accurately produce the chaotic lensed region, a better integration routine is required close to the event horizon.

The observation that the Cash-Karp integrator performs better than the Dormand-Prince integrator leads one to believe that the system of ODEs is stiff, with some parts of the system of equations growing much faster than the others. This is understandable, since g_{rr} becomes singular at the horizon whereas other components of the metric do not typically undergo violent oscillation. For these kinds of stiff ODE problems, implicit multi-step ODE solvers are preferable to explicit Runge Kutta Methods [13]. The lowest order case for such an integration style is the implicit Euler method, which for the differential

¹Thanks to Dr. Lucas Collodel for providing the Julia routine

²Thanks to Dr. Galin Gyulchev for providing these high resolution images with his independent handwritten Mathematica code

equation

$$\frac{dy}{dx} = f(x, y), \quad (6.16)$$

has the recurrence relation,

$$y_{n+1} = y_n + f(x_{n+1}, y_{n+1})dx. \quad (6.17)$$

The higher order recurrence relations can be derived using a polynomial fit, as one usually does for multi-step ODE solvers, such as the Adams Methods. Implementing a good geodesic integrator which conserves the Hamiltonian better for photons with impact parameter within the chaotic lensed region is the next milestone of this work.

An another interesting example which requires more investigation is the case of KBHSH which have heavy hair content ($q \approx 1$), but their shadows resemble standard Kerr, or even Schwarzschild-like black holes. An example is presented in Figure 6.5. The first row contains a comparison between the KBHSH with its Kerr equivalent, when ADM mass and angular momentum are used. The KBHSH appears very small and seems to resemble a Kerr black hole. The second row contains the image for the case when hole mass and angular momentum are used for comparison, and in this case the KBHSH retains its Kerr-like properties but the Kerr black hole used for comparison appears Schwarzschild thanks to a very small value of the normalized angular momentum a . Neither situation completely describes the shadow of this KBHSH. The relevant hole and hair quantities for each KBHSH explored in this section are provided in Table 6.2, and the Hamiltonian heat maps are presented in Figure 6.6. From the heatmaps it is clear that the chaotic shadows in Figure 6.4 suffer from large numeric error in the heavily lensed region, with the deviation of the average Hamiltonian going larger than even unity (10^0). The heatmaps for the KBHSH which appears to have a Kerr-like shadow has better performing Hamiltonian, owing to the lack of heavy chaotic lensing.

κ	M	J	M_h	M_ψ	J_h	J_ψ
0	0.360	0.277	0.085	0.275	0.002	0.275
-1	1.003	0.921	0.004	0.990	0	0.921
5	1.202	1.153	0.003	1.203	0	0.153
-5	0.921	0.833	0.004	0.880	0	0.833

Table 6.2: ADM, hole and field masses and angular momenta for the KBHSH whose shadows are shown in Figures 6.4 and 6.5. In some cases, the ADM quantities are not the direct sum of hole and hair quantities because of the numeric nature of the integrals required to ascertain these values.

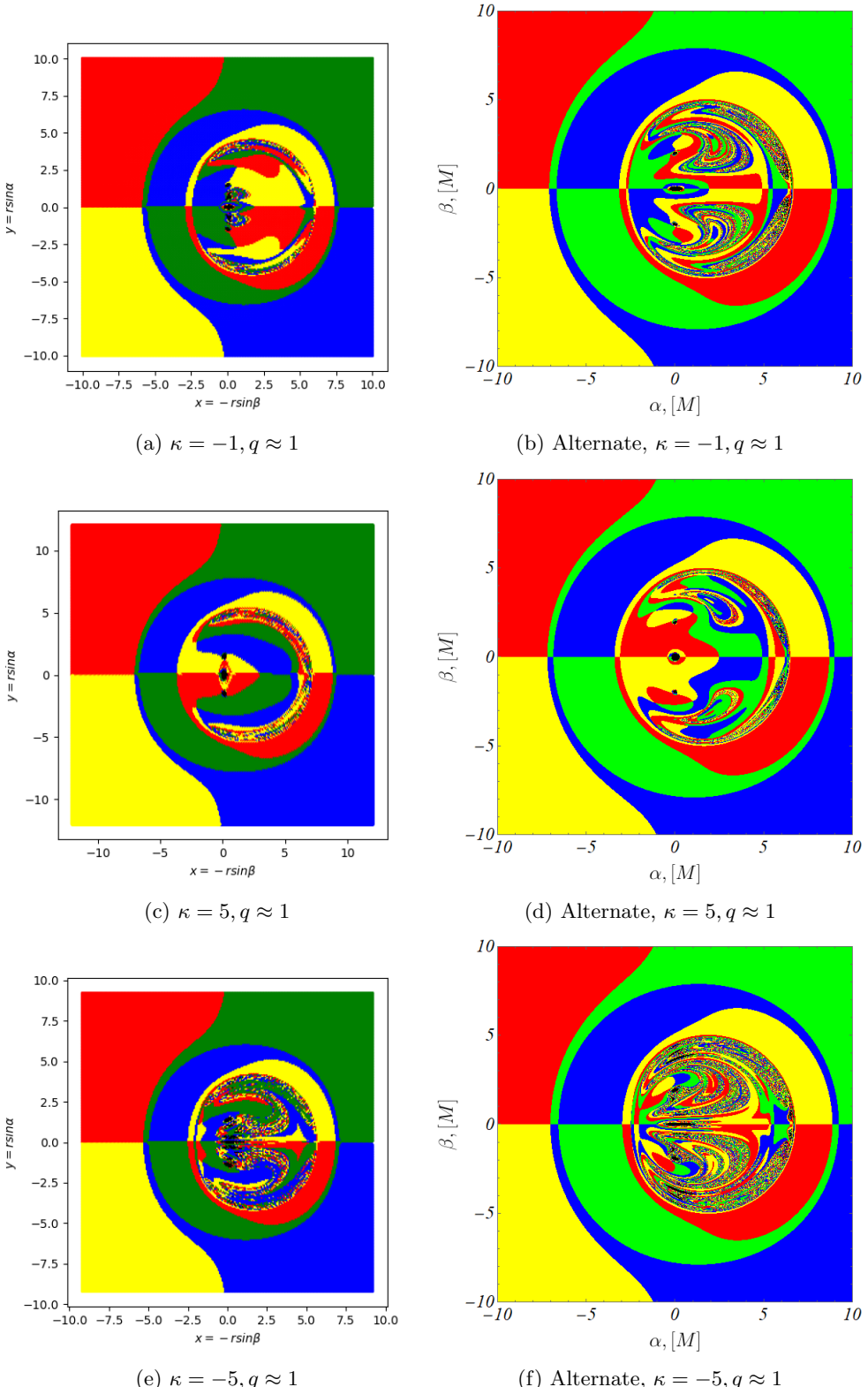


Figure 6.4: Chaotic shadows for KBHSH which are hair-dominated. On the left column are shadows produced by the code used for this thesis, and the right column shows true results made by independent external Mathematica code which has been credited in footnote 2. The observer is located at ($r = 15M, \theta = \frac{\pi}{2}, \phi = 0$). The relevant hole and hair quantities are listed in Table 6.2.

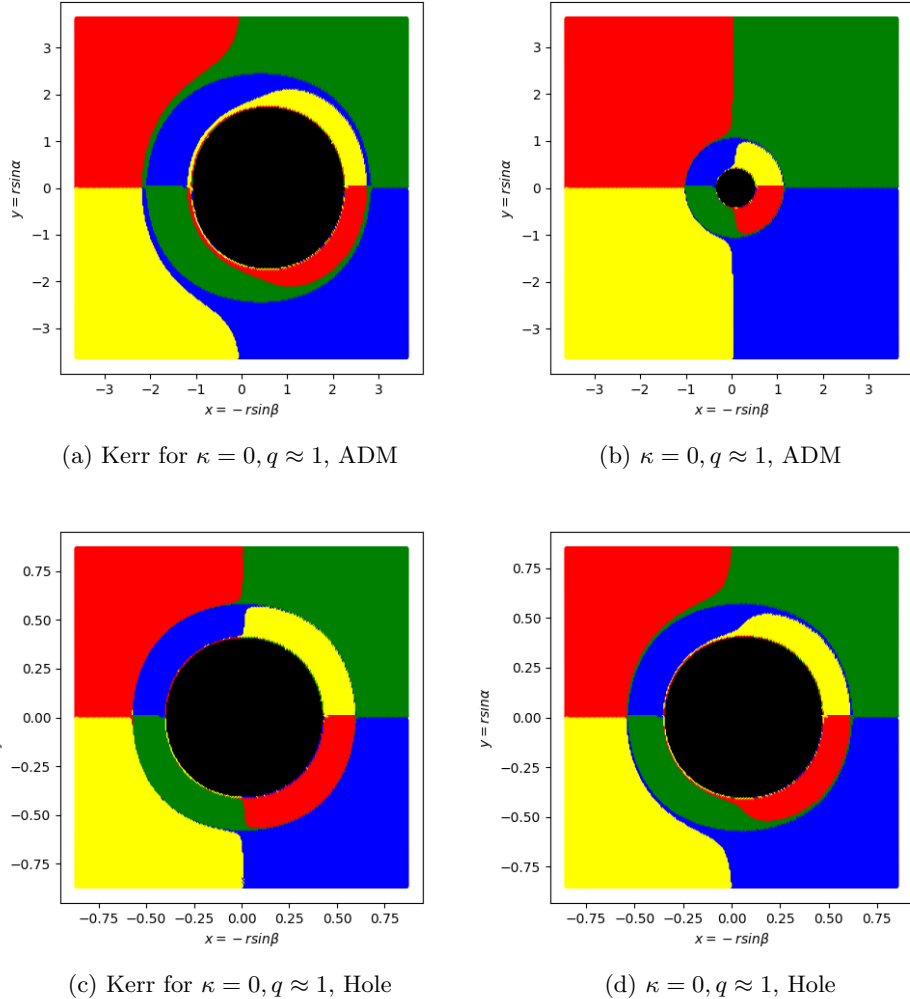


Figure 6.5: Comparison between Kerr and KBHSH shadows for an example case with $\kappa = 0, q \approx 1$. On the first row is the comparison considering ADM quantities, and the second row is the comparison considering hole quantities. The observer is located at $(r = 15M, \theta = \frac{\pi}{2}, \phi = 0)$. This is an interesting case where a KBHSH with $q \approx 1$ resembles a small Kerr black hole, but neither the ADM or hole equivalent Kerr black hole mimics its behaviour completely. The relevant hole and hair quantities are listed in Table 6.2.

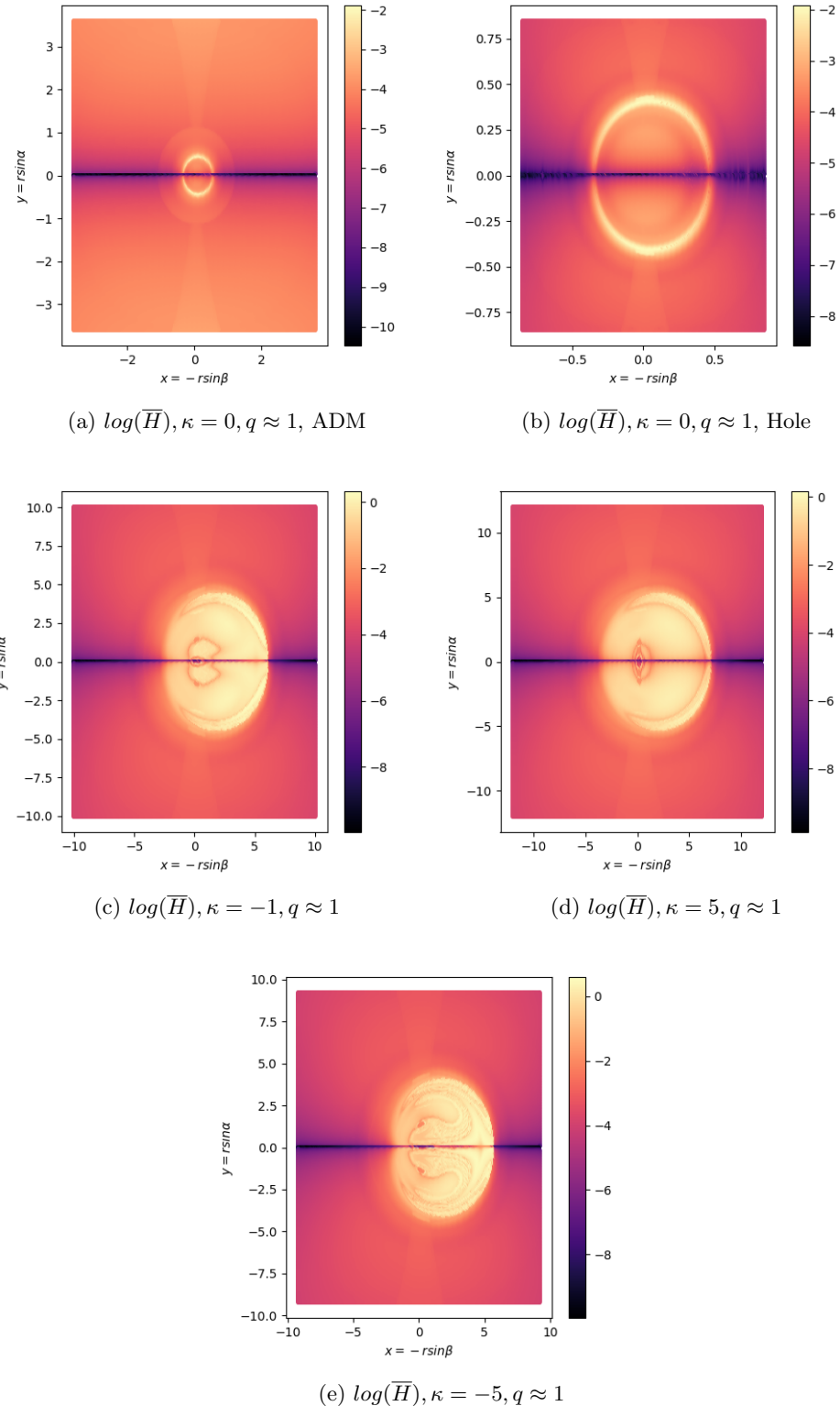


Figure 6.6: Deviation in the Hamiltonian \bar{H} for the shadows of KBHSH with $q \approx 1$, shown in the second column of Figures 6.4 and 6.5; the average Hamiltonian is shown in the log scale. Areas close to the rim of the shadow produce the most error. It is evident that KBHSH with a chaotic lensed region has a poorly performing Hamiltonian in general, with some pixels overshooting $10^0 = 1$ for their averaged Hamiltonian.

Chapter 7

Conclusion

Two standard spacetimes in the Theory of General Relativity are the Schwarzschild spacetime and the Kerr spacetime. The former models a spherically symmetric and static star or blackhole, where as the latter describes the spacetime surrounding a rotating blackhole. In the Schwarzschild case, interesting orbits for massive particles occur only when the conserved angular momentum per unit mass satisfies $l \geq \sqrt{12}M$. This condition is lifted for photons that have a fixed shape for the effective potential and an unstable circular orbit at $r = 3M$. Geodesic motion in Kerr spacetime is more complex, and some notable features include the structure of the photon region and the existence of the ergoregion caused due to frame dragging.

While the shadows for Schwarzschild black holes look circular, Kerr black holes have their shadows dragged to resemble the alphabet D. Prototypical geodesic motion and the shadows of both these standard spacetimes were computationally created using an explicit Cash-Karp Runge Kutta style of ODE integration. To make the shadows, orthonormal decomposition was used to set initial conditions and the results matched analytical expectations. Error analysis was also performed, and it was observed that a narrow band of photons at the centre of the observer's screen accumulates the largest error due to large initial velocities which can render the numerical scheme unstable.

Making shadows is especially of importance today, as the EHT collaboration has proven successful in capturing the image of $M87$ and more recently SgrA^* , showing their lensed background and other properties. Comparing these images with the results of gravitational theories will allow us to establish the validity of our scientific understanding. Therefore, it makes sense to consider well-posed theories of gravity that depart from General Relativity.

A simple and intuitive way to modify a theory in physics is to change its action, and such is done when considering general tensor multi-scalar theories of gravity. The special case considered was the two-scalar field theory of gravity. Spacetime solutions in this framework interpolate between the standard Kerr solutions in General Relativity, and completely new self-gravitating objects that are scalar field dominated such as boson stars. These scalar fields acting as additional degrees of freedom are expected to modify the shadows of their Kerr counterparts more significantly as the amount of scalar field contribution is increased. After developing a bicubic spline interpolation routine to tackle the numeric nature of the metric, a comparison was done with mock Kerr data, and the shadows produced were identical.

Lastly, shadows were created for the KBHSH found by Collodel et al. starting with the cloud case. As expected, these solutions with very low scalar field have coincidental shadows to their Kerr counterparts with horizon areas coinciding to the fourth decimal place, but adding more scalar field content leads to a chaotic lensed region which was difficult to reproduce accurately due to photons exhibiting complicated trajectories close to the horizon. It was also observed that this chaotic lensing is not experienced by every single KBHSH that is hair dominated ($q \approx 1$). It remains to be investigated which are the influential properties of the given KBHSH that shape its shadow, and how individual properties such as the mass, angular momentum, horizon radius, horizon frequency and Gaussian curvature play a role. A proposed future line of work is to analyze the effective potential of the photons that are shot backwards for ray tracing, to see the forbidden and allowed regions explicitly.

The quest to uncover and predict how particles move has lead physics to make some outstanding discoveries. While it is up for question, the apple performing geodesic motion and falling on Newton's head is picturesquely said to have inspired him to develop classical gravity. Also, Einstein's famous elevator thought experiment had the motion of light in different reference frames as its central theme. Now still in the 21st century, the EHT project requires an accurate understanding of how a multitude of photons move from the background space to the observer to compare the telescope's raw data. It is to be seen what new scientific findings will be born from this investigation into geodesic motion.

Bibliography

- [1] Benjamin P Abbott, Richard Abbott, TDe Abbott, MR Abernathy, Fausto Acernese, Kendall Ackley, Carl Adams, Thomas Adams, Paolo Addesso, RX Adhikari, et al. Observation of gravitational waves from a binary black hole merger. *Physical review letters*, 116(6):061102, 2016.
- [2] Fabio Bacchini, Bart Ripperda, Alexander Yuran Chen, and Lorenzo Sironi. Generalized, energy-conserving numerical simulations of particles in general relativity. i. time-like and null geodesics. *The Astrophysical Journal Supplement Series*, 237(1):6, 2018.
- [3] Carolina L Benone, Luís CB Crispino, Carlos Herdeiro, and Eugen Radu. Kerr-newman scalar clouds. *Physical Review D*, 90(10):104024, 2014.
- [4] Vitor Cardoso and Leonardo Gualtieri. Testing the black hole ‘no-hair’ hypothesis. *Classical and Quantum Gravity*, 33(17):174001, 2016.
- [5] Gregorio Carullo, Laura van der Schaaf, Lionel London, Peter TH Pang, Ka Wa Tsang, Otto A Hannuksela, Jeroen Meidam, Michalis Agathos, Anuradha Samajdar, Archisman Ghosh, et al. Empirical tests of the black hole no-hair conjecture using gravitational-wave observations. *Physical Review D*, 98(10):104020, 2018.
- [6] Carla Cederbaum and Sophia Jahns. Geometry and topology of the kerr photon region in the phase space. *General Relativity and Gravitation*, 51(6):79, 2019.
- [7] Event Horizon Telescope Collaboration et al. First m87 event horizon telescope results. iv. imaging the central supermassive black hole. *arXiv preprint arXiv:1906.11241*, 2019.
- [8] Event Horizon Telescope Collaboration et al. First sagittarius a* event horizon telescope results. ii. eht and multiwavelength observations, data processing, and calibration. 2022.
- [9] Lucas G Collodel, Daniela D Doneva, and Stoytcho S Yazadjiev. Rotating tensor-multiscalar black holes with two scalars. *Physical Review D*, 102(8):084032, 2020.
- [10] Lucas G Collodel, Daniela D Doneva, and Stoytcho S Yazadjiev. Rotating tensor-multiscalar solitons. *Physical Review D*, 101(4):044021, 2020.
- [11] Pedro VP Cunha, Carlos AR Herdeiro, Eugen Radu, and Helgi F Rúnarsson. Shadows of kerr black holes with scalar hair. *Physical review letters*, 115(21):211102, 2015.
- [12] Pedro VP Cunha, Carlos AR Herdeiro, Eugen Radu, and Helgi F Runarsson. Shadows of kerr black holes with and without scalar hair. *International Journal of Modern Physics D*, 25(09):1641021, 2016.
- [13] Charles Francis Curtiss and Joseph O Hirschfelder. Integration of stiff equations. *Proceedings of the National Academy of Sciences*, 38(3):235–243, 1952.
- [14] Thibault Damour. 1974: the discovery of the first binary pulsar. *Classical and Quantum Gravity*, 32(12):124009, 2015.
- [15] Thibault Damour and Gilles Esposito-Farese. Tensor-multi-scalar theories of gravitation. *Classical and Quantum Gravity*, 9(9):2093, 1992.
- [16] Kyriakos Destounis, Arthur G Suvorov, and Kostas D Kokkotas. Testing spacetime symmetry through gravitational waves from extreme-mass-ratio inspirals. *Physical Review D*, 102(6):064041, 2020.

- [17] Manfredo Perdigao Do Carmo and J Flaherty Francis. *Riemannian geometry*, volume 6. Springer, 1992.
- [18] Daniela D Doneva and Stoytcho S Yazadjiev. Mixed configurations of tensor-multiscalar solitons and neutron stars. *Physical Review D*, 101(2):024009, 2020.
- [19] Daniela D Doneva and Stoytcho S Yazadjiev. Nontopological spontaneously scalarized neutron stars in tensor-multiscalar theories of gravity. *Physical Review D*, 101(10):104010, 2020.
- [20] Daniela D Doneva and Stoytcho S Yazadjiev. Topological neutron stars in tensor-multi-scalar theories of gravity. *Physical Review D*, 101(6):064072, 2020.
- [21] Frank Watson Dyson, Arthur Stanley Eddington, and Charles Davidson. Ix. a determination of the deflection of light by the sun's gravitational field, from observations made at the total eclipse of may 29, 1919. *Philosophical Transactions of the Royal Society of London. Series A, Containing Papers of a Mathematical or Physical Character*, 220(571-581):291–333, 1920.
- [22] A Einstein. Explanation of the perihelion motion of mercury from the general theory of relativity. the collected papers of albert einstein. *Princeton University*, 6:112–116, 1997.
- [23] Valerio Faraoni. Illusions of general relativity in brans-dicke gravity. *Physical Review D*, 59(8):084021, 1999.
- [24] Andrea M Ghez, BL Klein, M Morris, and EE Becklin. High proper-motion stars in the vicinity of sagittarius a*: Evidence for a supermassive black hole at the center of our galaxy. *The Astrophysical Journal*, 509(2):678, 1998.
- [25] James B Hartle. Gravity: an introduction to einstein's general relativity, 2003.
- [26] Carlos Herdeiro and Eugen Radu. Construction and physical properties of kerr black holes with scalar hair. *Classical and Quantum Gravity*, 32(14):144001, 2015.
- [27] Carlos AR Herdeiro and Eugen Radu. Kerr black holes with scalar hair. *Physical review letters*, 112(22):221101, 2014.
- [28] Carlos AR Herdeiro and Eugen Radu. Asymptotically flat black holes with scalar hair: a review. *International Journal of Modern Physics D*, 24(09):1542014, 2015.
- [29] Markus Heusler. No-hair theorems and black holes with hair. *arXiv preprint gr-qc/9610019*, 1996.
- [30] Antony Hewish. Pulsars and high density physics. *Science*, 188(4193):1079–1083, 1975.
- [31] Shahar Hod. Stationary scalar clouds around rotating black holes. *Physical Review D*, 86(10):104026, 2012.
- [32] Shahar Hod. Stationary resonances of rapidly-rotating kerr black holes. *The European Physical Journal C*, 73:1–5, 2013.
- [33] Shahar Hod. The large-mass limit of cloudy black holes. *Classical and Quantum Gravity*, 32(13):134002, 2015.
- [34] Michael Horbatsch, Hector O Silva, Davide Gerosa, Paolo Pani, Emanuele Berti, Leonardo Gualtieri, and Ulrich Sperhake. Tensor-multi-scalar theories: relativistic stars and 3+ 1 decomposition. *Classical and Quantum Gravity*, 32(20):204001, 2015.
- [35] FD Lora-Clavijo, OM Pimentel, et al. Osiris: A new code for ray tracing around compact objects. *arXiv preprint arXiv:2202.00086*, 2022.
- [36] William H Press and Saul A Teukolsky. *Numerical recipes 3rd edition: The art of scientific computing*. Cambridge university press, 2007.
- [37] David Robinson. Four decades of black holes uniqueness theorems. *The Kerr spacetime: Rotating black holes in general relativity*, pages 115–143, 2009.
- [38] Irwin I Shapiro. Fourth test of general relativity. *Physical Review Letters*, 13(26):789, 1964.

- [39] Stoytcho S Yazadjiev and Daniela D Doneva. Dark compact objects in massive tensor-multi-scalar theories of gravity. *Physical Review D*, 99(8):084011, 2019.
- [40] AC Yew. Numerical differentiation: finite differences. *Brown University: Providence, RI, USA*, 2011.